A Systematic Measurement of Performances of Compensated Lead/Plastic-Scintillator Tile/Fiber Calorimeter

2000/Nov/06 version 0.90

S.Uozumi[a,1] T.Asakawa[a,2] J.P.Done[b] Y.Fujii[c,3] K.Furukawa[d,4] T.Ishizaki[a,5] S.Kaga[d,6] F.Kajino[e] T.Kamon[b] N.Kanaya[f,7] J.Kanzaki[c] S.Kim[a] K.Kawagoe[f] A.Nakagawa[a,8] M.Nozaki[f] R.Oishi[a,9] T.Ota[a,10] H.Takeda[f] T.Takeshita[d] A.Takeuchi[f,11] Y.Sugimoto[f,12]

[a] *Institute of Physics, University of Tsukuba, Tsukuba, Ibaraki 305-8571, Japan*
[b] *Department of Physics, Texas A&M University, College Station TX77843-4242, USA*
[c] *Institute of Particle and Nuclear Studies, High Energy Accelerator Organization(KEK), Tsukuba, Ibaraki 305-0801, Japan*
[d] *Department of Physics, Shinshu University, Matsumoto, Nagano 390-8621, Japan*
[e] *Department of Physics, Konan University, Kobe, Hyogo 658-8501, Japan*
[f] *Department of Physics, Kobe University, Kobe, Hyogo 657-8501, Japan*

Abstract

We have measured a performance of a lead-plastic scintillator sampling calorimeter in two separate low (1-4 GeV) and high (10-200 GeV) energy test beams . The calorimeter is composed of 8 mm-thick lead plates and 2mm-thick scintillator plates for hardware compensation where the responses to electromagnetic and hadronic showers of the same energy are the same. We find the linearity to be better than 1% between 2 GeV and 150 GeV for both pions and electrons, its energy resolutions of $(46.7 \pm 0.7)\%/\sqrt{E} \oplus (0.8 \pm 0.9)\%$ for pions and $(23.8 \pm 0.4)\%/\sqrt{E} \oplus (0.7 \pm 0.4)\%$ for electrons, and the response ratio of EM shower to hadronic shower to be 1.04.

[1]Corresponding author, e-mail : satoru@hepsg1.px.tsukuba.ac.jp
[2]present address : Yokogawa-denki, Yamanashi, Kofu, Japan
[3]Contact Person, Tel.+81-298-64-5369, e-mail yoshiaki.fujii@kek.jp
[4]present address : ???, Furukawa-san, Japan
[5]present address : FUJITSU LIMITED, Akiruno,Tokyo, Japan
[6]present address : Kaga-san, ???, Japan
[7]present address : CERN, CH-1211, Geneva, Switzerland
[8]present address : Media Technology, ????, ????, Japan
[9]present address : Ebara-Sangyo, Kawasaki, Kanagawa 211-0012, Japan
[10]present address : Nintendo Co.Ltd., Higashiyama-ku, Kyoto 605-8660, Japan
[11]present address : ???, Takeuchi-san, Japan
[12]present address : ???, Sugimoto-san, Japan

1 Introduction

In order to discover and perform precision study of higgs boson and to search for physics beyond the standard model, R&D's of e^+e^- linear colliders are extensively carried out in many high energy laboratories. The linear colliders will provide very clear experiment owing to their clearness of elementary processes. However in order to fully take advantage of their clearness, detectors of the most excellent performance are indispensable[1]. For the calorimetry, in order to distinguish W and Z bosons using their reconstructed 2-jet masses, following energy resolutions are required;

$$\sigma_{\mathrm{E}}/\mathrm{E} = 40\%/\sqrt{\mathrm{E}} \oplus 2\% \quad \text{for Hadrons, and}$$

$$\sigma_{\mathrm{E}}/\mathrm{E} = 15\%/\sqrt{\mathrm{E}} \oplus 1\% \quad \text{for EM particles.}$$

Here $\oplus$ means quadratic sum.

Hadronic energy resolution required above can only be achieved by compensated calorimeter ; either by hardware compensation or by software compensation. We adopted hardware compensation as a primary candidate from the view point of cost and density. In addition to this excellent hadron energy resolution, hardware compensation gives very nice performances such as Gaussian pulse height distribution and excellent linearity. Low photon yield, on the other hand, shall not be a problem for hadron calorimeter.

Extensive generic studies were carried out on the configuration which can achieve precise compensation[2]. Based on the study, we have built a tile/fiber hadron calorimeter module of realistic design, and carried out series of beam tests at KEK and at FNAL.

In this article we report the beam test results of the compensated tile/fiber hadron calorimeter. In section 2, the test module design are briefly described. In section 3, outline of the beam tests are described. We discuss the results of both experiments in section 4, and conclusions are given in section 5.

2 Calorimeter Module

The calorimeter module is a sampling calorimeter made of lead plates and plastic scintillator plates. It has a hanging-file structure, and lead plates and plastic scintillator assembly are hung over a pair of supporting beams as shown in Fig.1. The thicknesses of the lead and plastic scintillator plates are 8 mm and 2 mm, respectively, which is close enough to compensation ratio of 9:2[2]. The module has a transverse size of 1 m $\times$ 1 m to well-contain hadron showers.

The calorimeter module consists of front part and rear part. The front part (FCAL hereafter) is a σ-loop type tile/fiber calorimeter with 5×5 tower structure. The configuration of FCAL is shown in Fig.2. It is divided into 4

sections in longitudinal direction. Each section has 20 layers of lead plates and scintillator tiles, and thus has thickness of $1\lambda_I$ (interaction length).

The layout of the scintillator tile assembly is schematically shown in Fig.3. 25 scintillator tiles are arranged on a fiber-routing plate in 5×5 to form tower structure, and sandwiched with white PET films. Each scintillator tile, made of Kuraray SCSN-38, has size of 20 cm $\times$ 20 cm $\times$ 2 mm-thick, and four-sides are painted white with TiO_2-based emulsion. It has a σ-shaped groove with key-hole cross section, and a 1mm-ϕ WLS fiber with Y11-die is embedded in it. The WLS fiber is connected to a clear fiber at the exit from the tile groove with heat-splicing (ref [3]). The clear fibers are arranged on the fiber-routing plate as shown in Fig.3. They are then connected to clear-fiber bundles which runs to PMTs. Just before the connection to the PMTs, re-arrangement of fibers are done to make layer-based fiber assemblies to tower-based ones.

In the low energy beamtest at KEK (T411), PMTs Hamamatsu H1949 were used for all sections. On the other hand the in high energy beamtest at FNAL (T912), fine-mesh PMTs H6614-01 were used for sections 1 and 2 of the central tower to avoid saturation.

The fiber routing plates, made of 2 mm-thick acryl, are known to affect compensation very little as a result of a beam test carried out prior to the fabrication of this module.

The rear part of the calorimeter (RCAL hereafter) does not have a tower structure. The configuration of rear calorimeter is shown in Fig 4. Each RCAL scintillator has 6 straight grooves, and WLS fibers are embedded in the grooves. Each end of each WLS fiber is spliced to a clear fiber at the side of the scintillator. Clear fibers from each side of five successive scintillators are bundled to make a superlayer, and run to PMTs.

In low energy beamtest (T411) RCAL had only 2 superlayers. The absorber thickness of the calorimeter is 4.2 λ_I in total in T411. On the other hand in high energy beamtest (T912), RCAL had 10 superlayers. The most downstream superlayer is without lead absorber to use as a leak-veto counter. In T912, therefore, total absorber thickness of calorimeter is 5.9 λ_I.

3 Beamtests

3.1 Low energy beamtest at KEK (T411)

3.1.1 Setup

The T411 beam test was carried out at $\pi 2$ beam line of KEK proton synchrotron in July 1998. It provides unseparated beam of momentum up to 4 GeV with momentum bite of 1% (FWHM).

The outline of the setup is shown in Fig.5. In addition to the three trigger scintillation counters (T1-T3), two gas Cerenkov counters (C1 and C2) for

electron identification and four drift chambers (D1-D4) for tracking of incoming particles were installed on the beam line. Another scintillation counter (M1) was located downstream of the calorimeter module for muon tagging. In order to trigger muons penetrating each tower for calibration purpose, the calorimeter module was sandwiched by a pair of muon matrix counters (MX1 and MX2). The structure of muon matrix counter is also shown in Fig.5.

The calorimeter module had 72 cm-thick lead in total, which corresponded to about 4.2 λ_I.

Three kinds of triggers were used for data taking. One is an inclusive trigger, which is a coincidence of three trigger counters T1&T2&T3. An electron trigger was built as coincidence of trigger counters and Cerenkov counters as T1&T2&T3&C1&C2. Muon triggers, T1&T2&T3&M1 and MX1&MX2, were used for calibration purpose. Precise particle identification was further carried out by offline analysis using pulse height data of these counters.

Data were taken for momentum of 1 GeV, 2 GeV, 3 GeV and 4 GeV for inclusive and for electron triggers. 2 GeV data were taken with muon triggers for tower-to-tower gain calibration. Signals from the beam line devices and the calorimeter module are read by CAMAC modules such as LeCroy 3377 multi-hit TDCs and 2249W charge-integrated ADCs. Digitized data was processed on a PC, and stored on hard disk.

3.1.2 Gain Calibration

In order to calibrate gain of each FCAL section and each RCAL superlayer, pulse height of penetrating muons is used.

For FCAL calibration, data were taken with 'defocused' beam condition to deliver muons to off-beam-axis towers. Offline analysis is done to pick up events in which one single muon penetrated the section to be calibrated. Following event selections are carried out to pick up muon events for FCAL calibration. Here MIP stands for a minimum-ionizing particle.

- The muon matrix counter at the upstream of the section to be calibrated should have signal of one MIP-equivalent.
- All of RCAL superlayer should have signal of one MIP-equivalent.
- Signals of any towers surrounding the tower to be calibrated should be consistent to pedestals.
- Both upstream and downstream sections in the same tower that the section to be calibrated belongs to should have signal of one MIP-equivalent.

RCAL calibration was done using central-tower beam-injection data. Event selection for RCAL calibration is as follows.

- Signals of any sections in any towers except for the central tower should be consistent to the pedestals.

- The central tower in the section 4 should have signal of one MIP-equivalent.
- The muon matrix counter at the downstream of calorimeter should have signal of one MIP-equivalent.
- All PMTs of RCAL should have signals well-separated from the pedestals.

Typical pulse height spectrum for muons after event selections above is shown in Fig.6. The upper is for the tower 1 at the corner, and lower is for tower 13 at the center of the module. These spectrum were fit by Gaussian function, and the calibration constants are defined as the peak position of the fitting result. Though the spectrum is slightly different from the Gaussian distribution at the higher-tail region, thus-obtained calibration constant is quite stable against fitting range variation and spectrum shape deform caused by photon yield difference of tiles. Consistency between the fit parameter and numerical mean is discussed in the section of high-energy beam test.

Statistical error of the calibration constants are shown in Fig.7. Central towers are calibrated within $\sim 2\%$, while peripheral towers have error of $\sim 4\%$ due to low statistics caused by the profile of defocused beam.

3.1.3 Event Selection for e, π Analyis

First, single-particle events are selected by requiring that all trigger counters must have signals of one MIP-equivalent. Afterwards particle identification is done using pulse height information of the Cerenkov counters, muon counters, and RCAL.

Electrons are identified using Cerenkov counter pulse height. Scatter plot of the pulse height of two Cerenkov counters are shown in Fig.8. Electrons are clearly separated from other particles. In addition, events in which RCAL has signals greater than 0.15MIP-equivalent are further rejected to reduce contamination due to knock-on reaction in Cerenkov counters. Fraction of muons and hadrons in thus-made electron sample is estimated to be less than 0.01 %.

Non-electron samples are made by requiring that both Cerenkov counters must have signals consistent to pedestals. Among the non-electron samples, muons are identified by pulse height of the muon counter behind the calorimeter module. Thus-made non-electron non-muon samples are defined as pion samples. Fraction of electrons and muons in the pion sample is estimated to be less than 0.1 % and 1 %, respectively. In 1 GeV beam, however, pion events cannot be discriminated from muon events clearly because 1 GeV muon does not penetrate the calorimeter through. Thus we decide not to use 1 GeV pion data for later analysis.

Pulse height distributions for 4 GeV electrons and for 4 GeV pions are shown in Fig.9. Energy resolution is obtained by Gauss-fit of the spectrum. Results of these fits are summarized in Table.1.

Additional event selection is done to see the effect of longitudinal shower leakage. Events in which most downstream superlayer of RCAL have no signal are classified as 'no-leak sample'. Responses of all-event sample and no-leak sample are compared to estimate performances of sufficiently-thick calormeter module.

3.1.4 Systematic Errors

Following effects have been evaluated as sources of systematic errors on linearity and energy resolution.

1. Statistical error of calibration constants.

2. Variation of lead plate thickness.
   Fig.10 shows a distribution of thickness of the lead plates. Thickness of four points of 25 lead plates were measured. The variation is measured to be about 1.3%.

3. Variation of average photon yield of scintillator tiles.
   Distribution of the average photo-electron yield of 2000 tiles used in FCAL and that of RCAL scintillator plates are shown in Fig.11. Those are measured with β-source using the same PMT. FCAL tiles have 14.6% variation and RCAL scintillators have 14.3% variation in terms of RMS.

4. Non-uniformity of response in each FCAL tile and RCAL scintillator.
   Response map of photo-electron yield in a FCAL tile is shown in Fig.12. The four corners have significantly low photon yield, while the area close to the WLS fibers has slightly high photon yield.

5. Phototube gain drift and fluctuation.
   Gain of PMTs are traced by two sets of LED monitors. From the data, this effect is estimated to have ?.? % effect at the maximum.

6. ADC pedestal drift and fluctuation.
   Pedestals are monitored continuously through the data taking at off-spill timing. The pedestal change is estimated to introduce error only on calibration constant of about ?.? %.

Effects of items 1, 2, 3 and 4 are evaluated with GEANT3 simulation with GHEISHA package. Cut-off energies of 10keV and 500keV are used for EM particles and for hadrons, respectively. The result of the simulation for the item 3 in the case of 3 GeV pion is shown in Fig.13. Deviation of energy resolution from the equal-photo-yield sample is plotted for 100 samples with photo-yield variation. In each sample, photo-yield of tiles are varied according

to the variation shown in Fig.11. It is seen that this variation has only 0.56%-effect on the energy resolution. The other major systematic error, variation of lead-thickness, has almost the same effect as discussed in refsuzuki.

Evaluated systematic errors are summarized in Table.4.

3.2 High-energy beam test at FNAL (T912)

3.2.1 Setup

The high-energy beam test (T912) was carried out at FNAL meson test beam line (MT6) in Sep 1999. Unseparated negative beams of 10 - 200 GeV were used. The setup of the experiment is schematically shown in Fig 14. A pair of single wire drift chambers (SWDC) were installed at both upstream and downstream of the final bending magnet to determine the particle momentum. Immediately at the downstream of the bending magnet, there was a synchrotron radiation detector (SRD) for electron identification. In front of the calorimeter, 3 trigger counters (T4,T5,TPSD) were installed to use for DAQ trigger and for offline event selection. The calorimeter module was placed on a moving stage which can move both horizontally and vertically. RCAL had 10 superlayers in T912. The most downstream superlayer did not contain lead absorbers, and was used for muon-tag and shower-leak veto. The calorimeter had 100 cm-thick lead in total, which corresponded to 5.9 λ_I. At the most downstream of the beamline, a muon counter was installed to identify muons.

Only an inclusive trigger, simple coincidence of two trigger scintillation counters T4 and T5, was used for all data taking. All event selections were done off-line. Electron and pion data, however, were taken by tuning the beam to be electron-rich and pion-rich conditions, respectively, by choosing proper radiator/absorber combinations for secondary beam. Pion-tuned beam contains about 5% of muons, and these muons were used for calibration.

Data were taken for nominal momentum of 10, 25, 50, 75, 100, 150 and 200 GeV for pion-tuned beams, and 10, 25, 50, 75, 100 and 150 GeV for electron-tuned beams. Muon events were taken with 50 GeV pion-tuned beam injected into the center of each tower to calibrate each section. When we were taking pion or muon events, a 50mm-thick (2.8 X_0) iron block was installed in front of the TPSD counter to reject electrons using its pulse height.

The signals of SWDCs and other detectors are read out via CAMAC system with such as LeCroy 3377 multi-hit TDCs and LeCroy 2280 ADC system. The data from CAMAC are then processed on PC-Linux machine, and stored on hard disk drives for offline analysis.

3.2.2 Gain Calibration

Gain calibration of each section of the FCAL was done using muons in pion-tuned event sample which penetrated each tower. Selection criteria of muon events from pion events are as follows.

- All trigger counters must have signal of one MIP-equivalent.
- Signals of any sections in the towers surrounding the tower to be calibrated should be consistent to pedestals.
- Most downstream superlayer of RCAL must have signal of one MIP-equivalent.

Muon sample for the central-tower calibration is also used to calibrate RCAL superlayers.

The typical muon pulse height distribution after event selection is shown in Fig 15. This spectrum has significant tail. These spectra are thus fit by Landau function, which is expressed as

$$f(x) = Ae^{-\frac{y+e^{-y}}{2}} \quad , \quad y = \frac{x-B}{C}$$

Calibration constant is defined by the parameter B. Statistical error of the calibration constant is shown in Fig 16. All towers are well calibrated within about 2%, and central towers have errors of less than 1.5%.

Consistency of calibration constants between numerical-mean definition and fit-parameter definition are examined. Distribution of the calibration constant ratio of mean/fit is shown in Fig 17. Upper plot is for each section of FCAL, and lower is for RCAL. Spread of the ratio for FCAL is about 2.9%, which is quite close to $\sqrt{2}\times$ statistical error of calibration constants. This means that systematic effects such as improper fitting function or channel-to channel change of spectra shape are not introduced into this fitting procedure. On the other hand, distribution for RCAL has about 5.1% spread, which is slightly worse than $\sqrt{2}\times$ statistical error . The reason is considered to be that some RCAL channels had larger electrical noise. Thus we adopted fit parameters to calculate calibration constants because of its robustness to electrical noise.

3.2.3 Beam Momentum Determination

In order to determine momentum of incoming particles, event-by-event tracking is done using two pairs of SWDCs located upstream and downstream of the final bending magnet. Typical reconstructed momentum distribution is shown in Fig.18 for electrons and in Fig.19 for pions. The dominant source of the width is thought to be reconstruction resolution, since actual spread of the beam momentum is calculated to be only 0.26% [9] for secondary beams (pion-tuned beams). For electron-tuned beams, however, beam momentum spread is not calculated.

Correspondence between the nominal momentum and actual (reconstructed) momentum and its spread is summarized in Table 2. A correlation plot between reconstructed particle momentum and particle energy measured by calorimeter is also shown in Figs.18 and 19. Weak positive correlation can be seen only

for electrons. We thus think that beam momentum spread of electron-tuned beams is significantly larger than that of pion-tuned beams. Energy resolution of the calorimeter with and without correction with reconstructed momentum is shown in Fig.20 for electrons and in Fig.21 for pions. Slight improvement is observed by correction for electrons. We thus make an event-by-event correction for particle momentum.

3.2.4 Event Selection For e^-, π^- Analysis

In T912 beamtest, beam contained a lot of multi-particle events which were caused by interaction of particles with beamline materials upstream of the calorimeter. In order to reject these events, we impose single-particle selections as follows as the first step of analysis before particle identification.

- All trigger counters (T4, T5 and TPSD) should have signals of one MIP-equivalent.
- The number of hits for each SWDC plane should be only one.
- SWDC timing signals should be in a band corresponding to a single-track area as shown in Fig.22.

After these cuts, particle identification is carried out using the muon counter, SRD, and calorimeter signals. Selection criteria for electrons are as follows.

- Signal of the muon counter should be consistent to the pedestal.
- Particle must deposit more than 99 % of its energy in the section 1 of FCAL.
- Signal of SRD must be well-above the pedestal as shown in Fig.23 for electrons which momentum is 75 GeV or higher.

Event selection criteria for pions are as follows.

- Sum of the signals over FCAL section 2,3,4 and RCAL must be larger than that of 0.6 MIP-equivalent.
  This cut rejects electron events.
- Sum of the signals over the whole calorimeter must be more than 3 MIP-equivalent.
  This cut rejects muon events.

An example of e/π separation using calorimeter signal is shown in Fig 24. Electrons and muons can be rejected from the pion sample very clearly. Typical energy spectrum for e^- and π^- after event selection are shown is Fig 25 for nominal energy of 50 GeV data. As a result of the hardware compensation, energy spectrum for pion follows Gaussian distribution very well. These spectra

are fit by Gaussian function to obtain energy resolution. Results of these fits are summarized in Table 3.

Similar to T411, additional event selection is done to see the effect of longitudinal shower leakage using pulse height of leak-veto superlayer of RCAL. Energy spectra for 200 GeV pions are shown in Fig.26 for all-event sample and for no-leak sample. Low-energy tail in all-event sample disappears in no-leak sample.

3.2.5 Systematic Errors

Following effects are evaluated as a source of systematic errors as in the case of T411.

1. Statistical error of calibration constant.
2. Variation of lead plate thickness.
3. Variation of average photon yield of scintillator tiles.
4. Non-uniformity of response in each FCAL and RCAL scintillator.
5. Phototube gain drift and fluctuation
   Gain of PMTs are traced by two sets of LED pulsers.
   In T912 effect is about ?.? % at the maximum.
6. ADC pedestal drift and fluctuation.
   This is negligiblly small in T912.

Effect from source 1, 2, 3 and 4 are evaluated with GEANT3 simulation with GHEISHA package.

Stability of bending magnet is quite excellent ($\sim 0.01\%$) except for the lowest momentum of 10 GeV, where 4% fluctuation was observed.

Systematic errors from these sources are summarized in Table 4.

4 Results

4.1 Energy resolution

Energy resolution for both T411 and T912 are plotted in Fig.27. Horizontal axis is $1/\sqrt{\mathrm{E}}$ for ease of interpretation. Energy dependence is obtained by fitting data with function of

$$\sigma_{\mathrm{E}}/\mathrm{E} = \sigma_{stochastic}/\sqrt{\mathrm{E}} \oplus \sigma_{constant}$$

The result of fitting is

$$\frac{\sigma_{\mathrm{E}}}{\sqrt{\mathrm{E}}} = \frac{46.7 \pm 0.7\%}{\sqrt{\mathrm{E}}} \oplus 0.8 \pm 0.9\% \quad \text{for } \pi^-$$

$$= \frac{23.8 \pm 0.4\%}{\sqrt{\mathrm{E}}} \oplus 0.7 \pm 0.4\% \quad \text{for } \mathrm{e}^-$$

Energy resolution for no-leak sample is shown in Fig.28. The same fitting gives pion energy resolution of

$$\frac{\sigma_{\mathrm{E}}}{\sqrt{\mathrm{E}}} = \frac{46.3 \pm 0.7\%}{\sqrt{\mathrm{E}}} \oplus 0.0^{+0.5}_{-0.0}\% \quad \text{for } \pi^-$$

Obtained resolution is significantly worse than the design value. This is not due to the longitudinal shower leakage since the stochastic term of the no-leak sample is almost the same as that of the all-event sample, while it has significant effect on the constant term.

4.2 Linearity

Linearity of energy measurement is shown in Fig.29. Relative normalization between T411 and T912 is done by 4 GeV electron data and 49.1 GeV electron data. Linearity for no-leak sample is also shown in Fig.30. 10 GeV data has large error due to the magnet current instability. Except for the 200 GeV data, linearity is about $\pm 1\%$ level. Linearity for no-leak sample improves significantly for low-energy region, but 200 GeV data still have significant deviation of $\sim 2\%$. It in unlikely that this is caused by saturation of PMTs since the deviation is observed not only for electrons and also for pions with almost same amount. Saturation of the bending magnet could have caused this effect.

Except for this 200 GeV data, we can conclude that linearity of $\pm$ 1% is achieved over energy range from 2 GeV to 150 GeV.

4.3 e/π energy ratio

The plot of the e/π energy ratio is shown in Fig.31. Unfortunately beam momentum for pions are slightly different from those for electrons. Since response of calorimeters to EM shower has better linearity than that to hadron showers, electron response is scaled to the pion beam momentum and e/π energy ratio is calculated.

At low energies, e/π ratio is about 1.04. This is consistent to the precise measurement of [2]. At high energies, e/π ratio becomes closer to one. This behaviour is consistent to the hadron shower mechanism in which more fraction of energy is transfered to π^0 production at higher energy.

5 Summary

We have measured energy resolution, linearity and e/π energy ratio of compensated tile/fiber hadron calorimeter test module in the energy range from 1GeV to 200GeV.

The energy resolution for pions is measured to be $\sigma/\mathrm{E} = 46.7 \pm 0.7\%/\mathrm{E} \oplus 0.8 \pm 0.9\%$ for all-event samples, and $\sigma/\mathrm{E} = 46.3 \pm 0.7\%/\mathrm{E} \oplus 0.0^{+0.5}_{-0.0}\%$ for no-leak samples. The reason for the worse resolution than the design value is under investigation.

Good linearity of $\sim \pm$ 1% is obtained for the energy range from 2GeV to 150GeV for no-leak samples.

This work is supported, in part, by Grant-in-Aid xxxxxxxx.

References

[1] JLC-I, JLC Group, KEK Report, **92-16** (1992).

[2] T. Suzuki *et al.*, Nucl. Instrum. Methods Phys. Res., Sect. **A 432** (1999) 48 - 65.

[3] K. Hara *et al.*, Nucl. Instrum. Methods Phys. Res., Sect. **A 348** (1994) 139.

[4] The CDF II Collaboration, The CDF II Detector Technical Design Report FERMILAB-Pub-**96/390-E** (1996).

[5] T. Asakawa *et al.*, Nucl. Instrum. Methods Phys. Res., Sect. **A 340** (1994) 458.

[6] S. Aota *et al.*, Nucl. Instrum. Methods Phys. Res., Sect. **A 352** (1995) 557.

[7] S. Kim (CDF Collaboration), Nucl. Instrum. Methods Phys. Res., Sect. **A 360** (1995) 206.

[8] S. Aota *et al.*, Nucl. Instrum. Methods Phys. Res., Sect. **A 357** (1995) 71.

[9] C.N.Brown and T.R.Kobilarcik, FERMILAB-TM-2108, May 2000

[10] K.Kawagoe *et al.*, to be submitted to Nucl. Instrum. Methods Phys. Res., Sect. **A**

Pion				Electron			
Beam momentum	σ/E	Stochastic error	Systematic error	Beam momentum	σ/E	Stochastic error	Systematic error
1 GeV	—	—	—	1 GeV	23.2 %	±0.3 %	± 0.8 %
2 GeV	32.7 %	±0.4 %	± 0.8 %	2 GeV	17.0 %	±0.2 %	± 0.6 %
3 GeV	27.5 %	±0.3 %	± 0.6 %	3 GeV	13.4 %	±0.1 %	± 0.4 %
4 GeV	23.8 %	±0.3 %	± 0.7 %	4 GeV	12.0 %	±0.1 %	± 0.4 %

Table 1: Energy resolution at the low-energy beam test (T411) at KEK.

Pion

Nominal momentum	Actual momentum	momentum spread (RMS)	Momentum systematic error	Bending magnet current
10 GeV	9.4 GeV	1.4 %	4.0 %	56.7 A
25 GeV	24.0 GeV	0.9 %	1.5 %	142.6 A
50 GeV	49.1 GeV	0.9 %	0.8 %	290.2 A
75 GeV	73.4 GeV	0.8 %	0.1 %	433.5 A
100 GeV	96.6 GeV	0.8 %	$\leq$ 0.1 %	568.5 A
150 GeV	146.6 GeV	0.9 %	0.1 %	864.9 A
200 GeV	200.8 GeV	0.7 %	0.3 %	1151.2 A

Electron

Nominal momentum	Actual momentum	momentum spread (RMS)	Momentum systematic error	Bending magnet current
10 GeV	9.2 GeV	1.4 %	2.3 %	55.1 A
25 GeV	27.8 GeV	1.6 %	1.2 %	163.5 A
50 GeV	55.5 GeV	1.5 %	0.1 %	325.5 A
75 GeV	83.2 GeV	1.6 %	0.1 %	489.1 A
100 GeV	101.2 GeV	1.4 %	0.3 %	598.4 A
150 GeV	187.7 GeV	1.3 %	0.4 %	1064.5 A

Table 2: Correspondence between moninal and actual (reconstructed) momentum .

Pion

Beam momentum	σ/E	Stochastic error	Systematic error
9.8 GeV	14.2 %	±0.4 %	0.7 %
23.9 GeV	9.2 %	±0.1 %	0.8 %
49.1 GeV	6.5 %	±0.1 %	0.5 %
73.4 GeV	5.5 %	±0.1 %	0.4 %
96.6 GeV	4.8 %	±0.1 %	0.5 %
146.6 GeV	4.0 %	±0.1 %	0.3 %
201.1 GeV	3.5 %	±0.1 %	0.3 %

Electron

Beam momentum	σ/E	Stochastic error	Systematic error
9.7 GeV	9.2 %	±0.4 %	0.6 %
27.7 GeV	4.9 %	±0.1 %	0.3 %
56.4 GeV	3.3 %	±0.1 %	0.2 %
84.4 GeV	2.7 %	±0.1 %	0.2 %
101.3 GeV	2.5 %	±0.1 %	0.2 %
187.9 GeV	1.9 %	±0.1 %	0.2 %

Table 3: Energy resolution at the high-energy beam test (T912) at FNAL.

Pion

Beam momentum	variation of lead plate	variation of scintillator photon yield	scintillator non-uniformity	PMT gain fluctuation	ADC pedestal fluctuation	statistical error of calibration
2 GeV	0.6 %	0.5 %	0.? %	0.? %	0.? %	0.? %
3 GeV	0.5 %	0.4 %	0.? %	0.? %	0.? %	0.? %
4 GeV	0.4 %	0.6 %	0.? %	0.? %	0.? %	0.? %
9.8 GeV	0.6 %	0.6 %	0.? %	0.? %	$\leq$ 0.1 %	0.1 %
23.9 GeV	0.3 %	0.4 %	0.? %	0.? %	$\leq$ 0.1 %	$\leq$ 0.1 %
49.1 GeV	0.4 %	0.2 %	0.? %	0.? %	$\leq$ 0.1 %	$\leq$ 0.1 %
73.4 GeV	0.3 %	0.3 %	0.? %	0.? %	$\leq$ 0.1 %	$\leq$ 0.1 %
96.6 GeV	0.4 %	0.2 %	0.? %	0.? %	$\leq$ 0.1 %	$\leq$ 0.1 %
146.6 GeV	0.2 %	0.2 %	0.? %	0.? %	$\leq$ 0.1 %	$\leq$ 0.1 %
201.1 GeV	0.3 %	0.2 %	0.? %	0.? %	$\leq$ 0.1 %	0.1 %

Electron

Beam momentum	variation of lead plate	variation of scintillator photon yield	scintillator non-uniformity	PMT gain fluctuation	ADC pedestal fluctuation	statistical error of calibration
1 GeV	0.5 %	0.7 %	0.? %	0.? %	0.? %	0.? %
2 GeV	0.4 %	0.4 %	0.? %	0.? %	0.? %	0.? %
3 GeV	0.3 %	0.3 %	0.? %	0.? %	0.? %	0.? %
4 GeV	0.3 %	0.2 %	0.? %	0.? %	0.? %	0.? %
9.8 GeV	0.4 %	0.4 %	0.? %	0.? %	$\leq$ 0.1 %	0.1 %
27.7 GeV	0.2 %	0.3 %	0.? %	0.? %	$\leq$ 0.1 %	$\leq$ 0.1 %
56.4 GeV	0.1 %	0.2 %	0.? %	0.? %	$\leq$ 0.1 %	$\leq$ 0.1 %
84.4 GeV	0.1 %	0.1 %	0.? %	0.? %	$\leq$ 0.1 %	$\leq$ 0.1 %
101.3 GeV	0.1 %	0.1 %	0.? %	0.? %	$\leq$ 0.1 %	$\leq$ 0.1 %
187.9 GeV	0.1 %	0.1 %	0.? %	0.? %	$\leq$ 0.1 %	$\leq$ 0.1 %

Table 4: Systematic errors of energy resolution ($\Delta(\sigma/\mathrm{E})$).

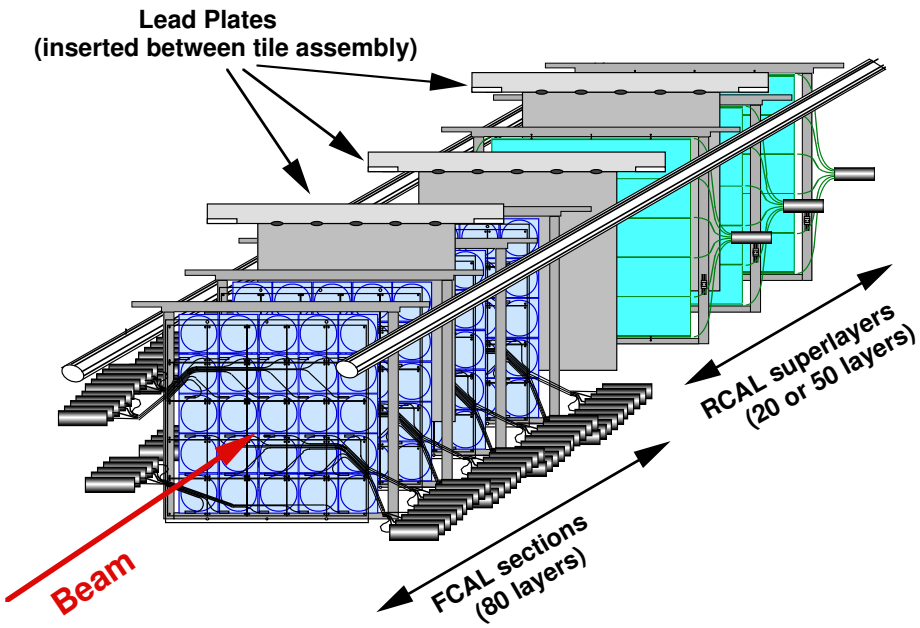

Figure 1: A schematic view of the calorimeter module.

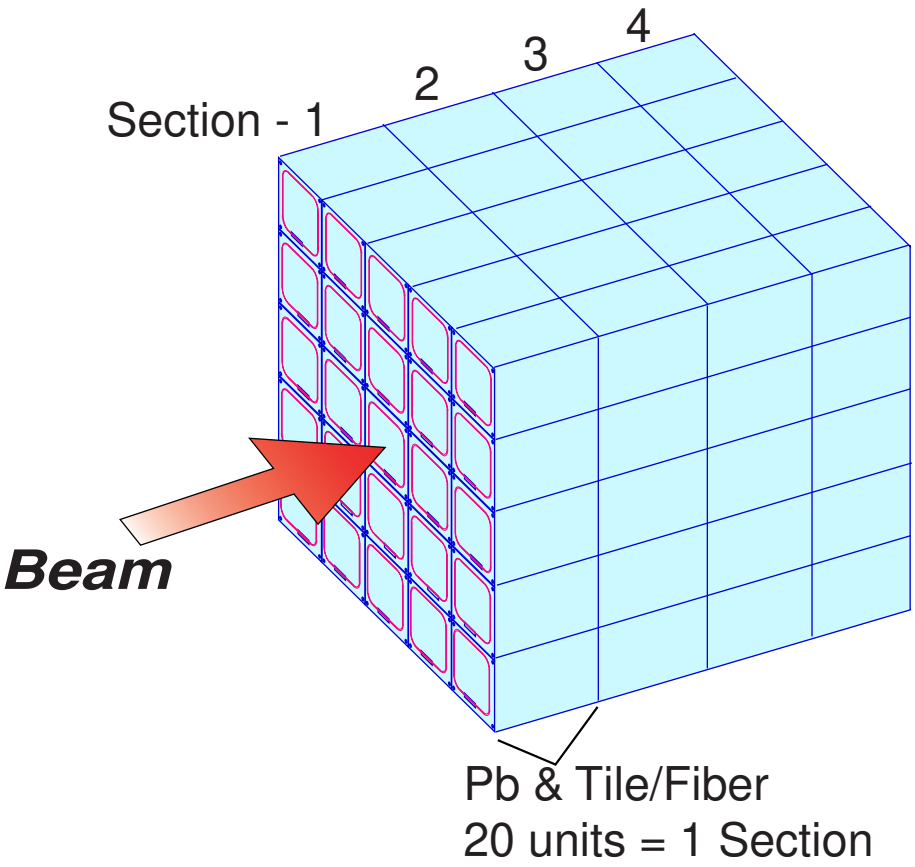

Figure 2: Segmentation scheme of the front part of the calorimeter (FCAL).

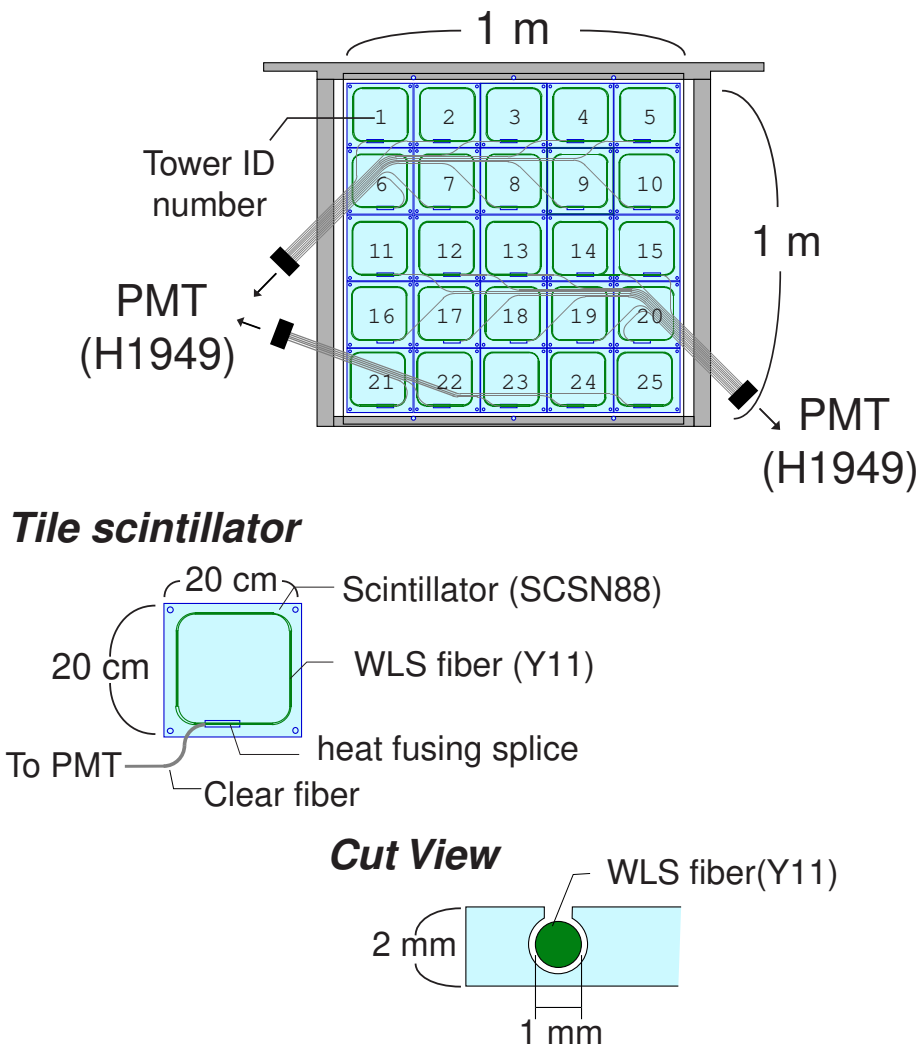

Figure 3: Optical configuration of the tile scintillator assembly used in FCAL.

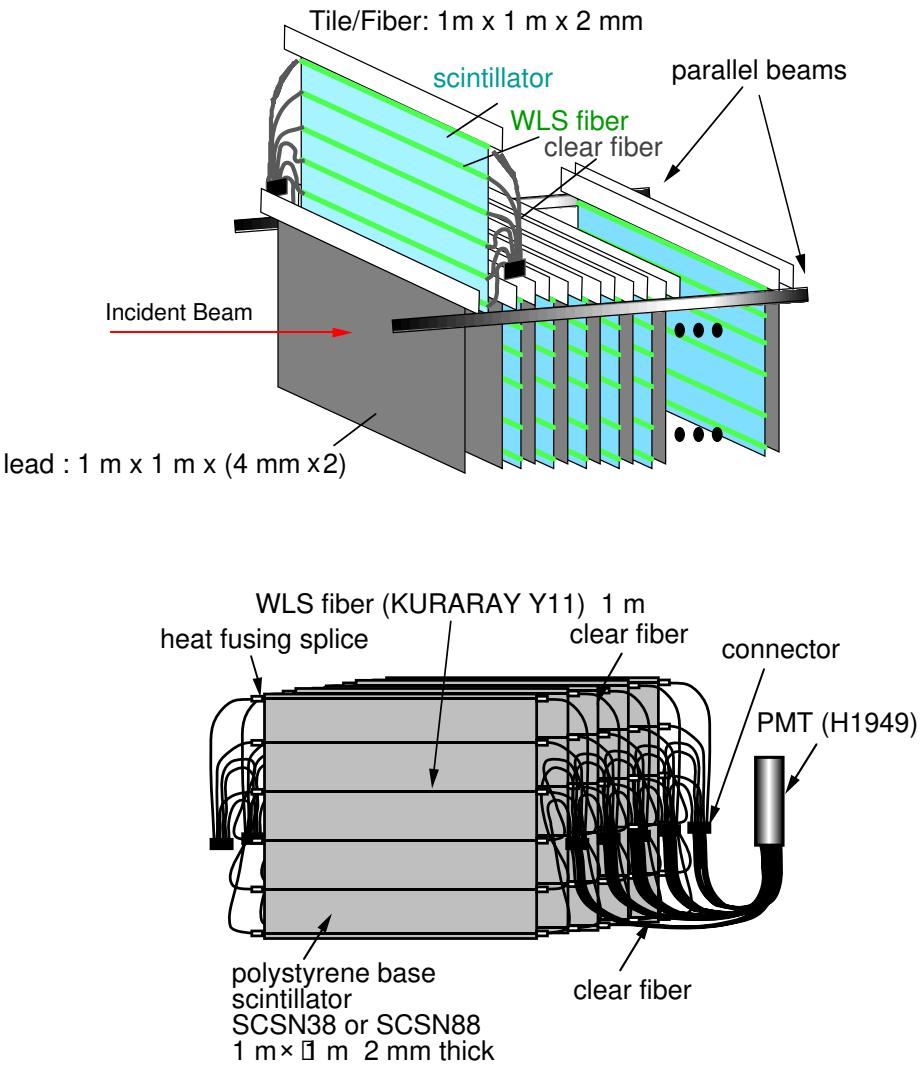

Figure 4: Configuration of the rear part of the calorimeter (RCAL).

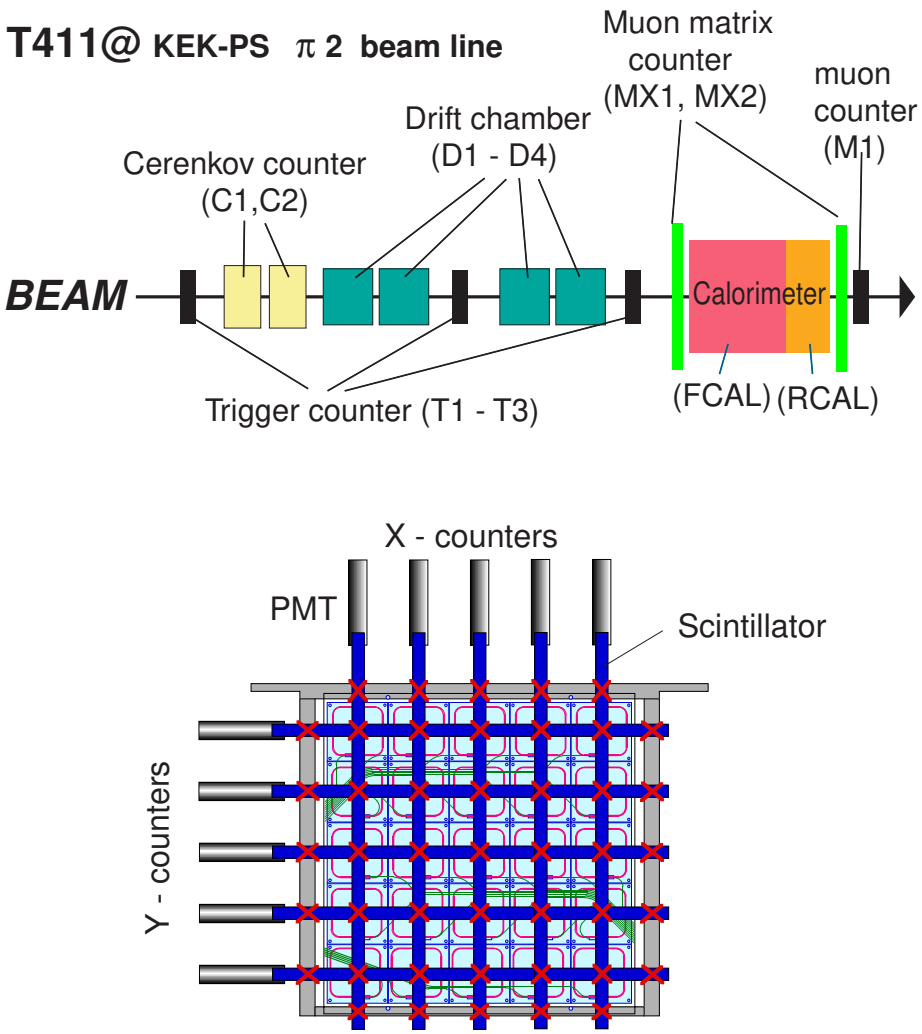

Figure 5: Layout of the T411 setup (upper), and structure of the muon matrix counter (lower).

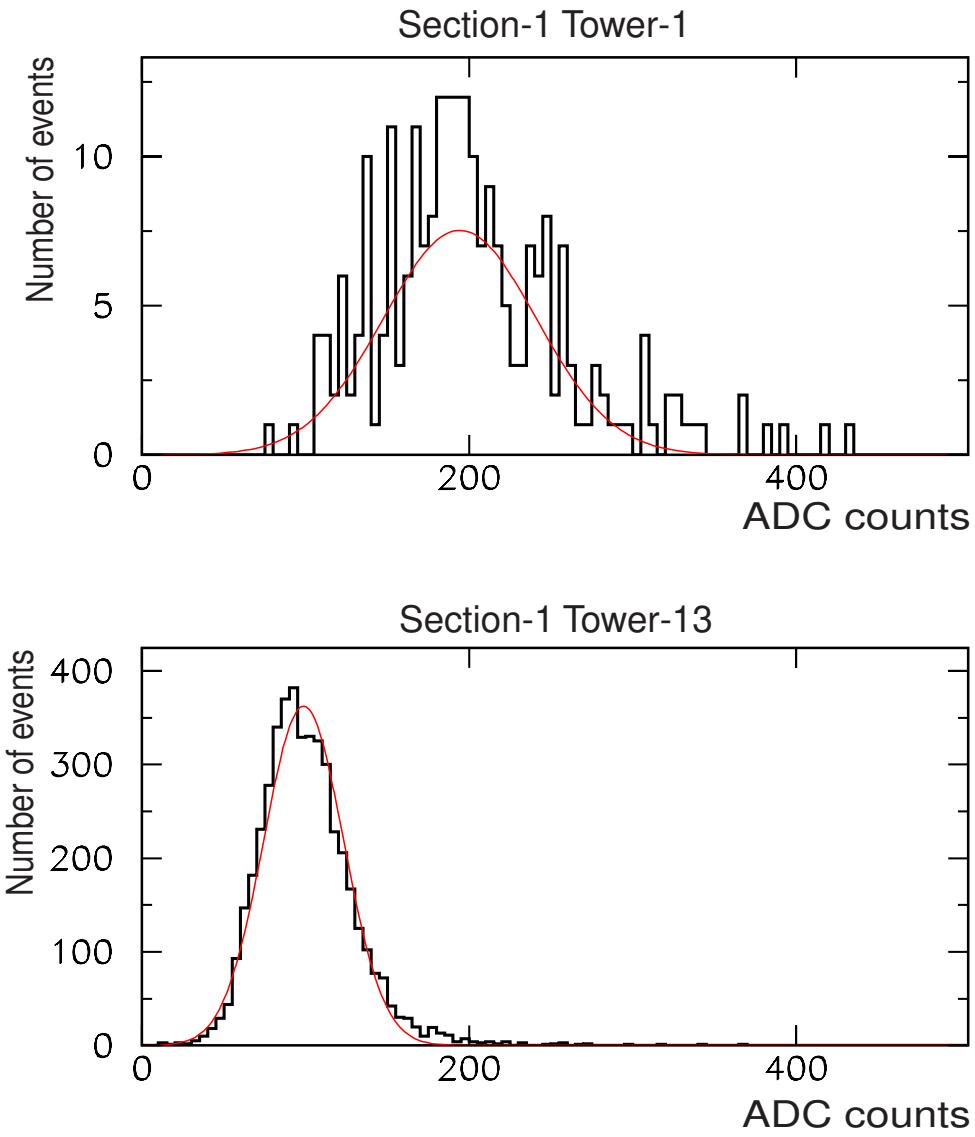

Figure 6: Typical pulse-height spectrum for muons. Upper is for tower 1 at the corner, and lower is for tower 13 at the center.

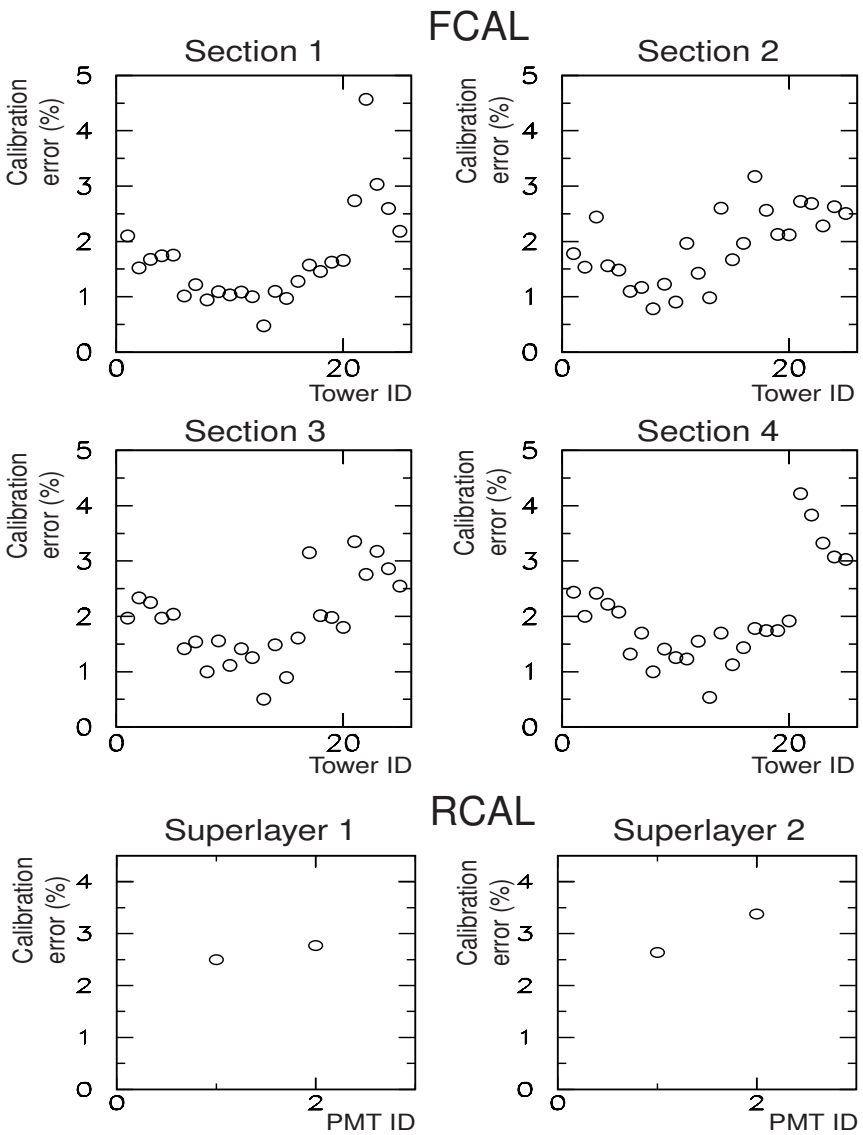

Figure 7: Stochastic error of the calibration constants.

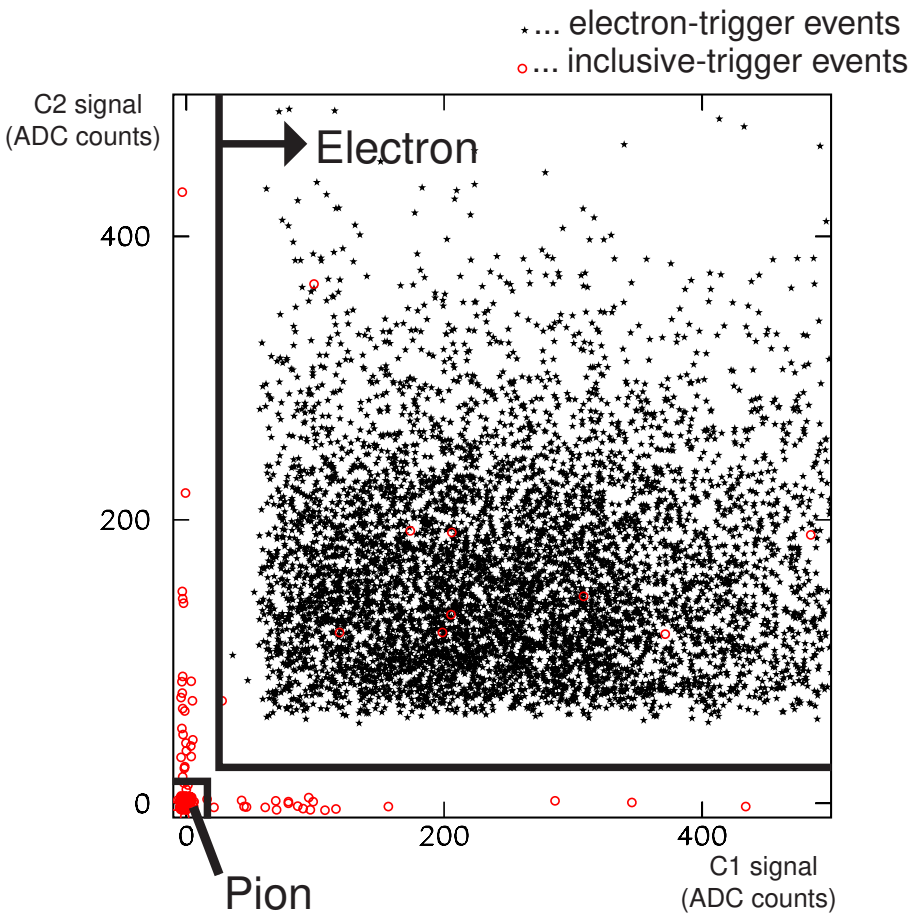

Figure 8: Pulse height of Cerenkov counters.

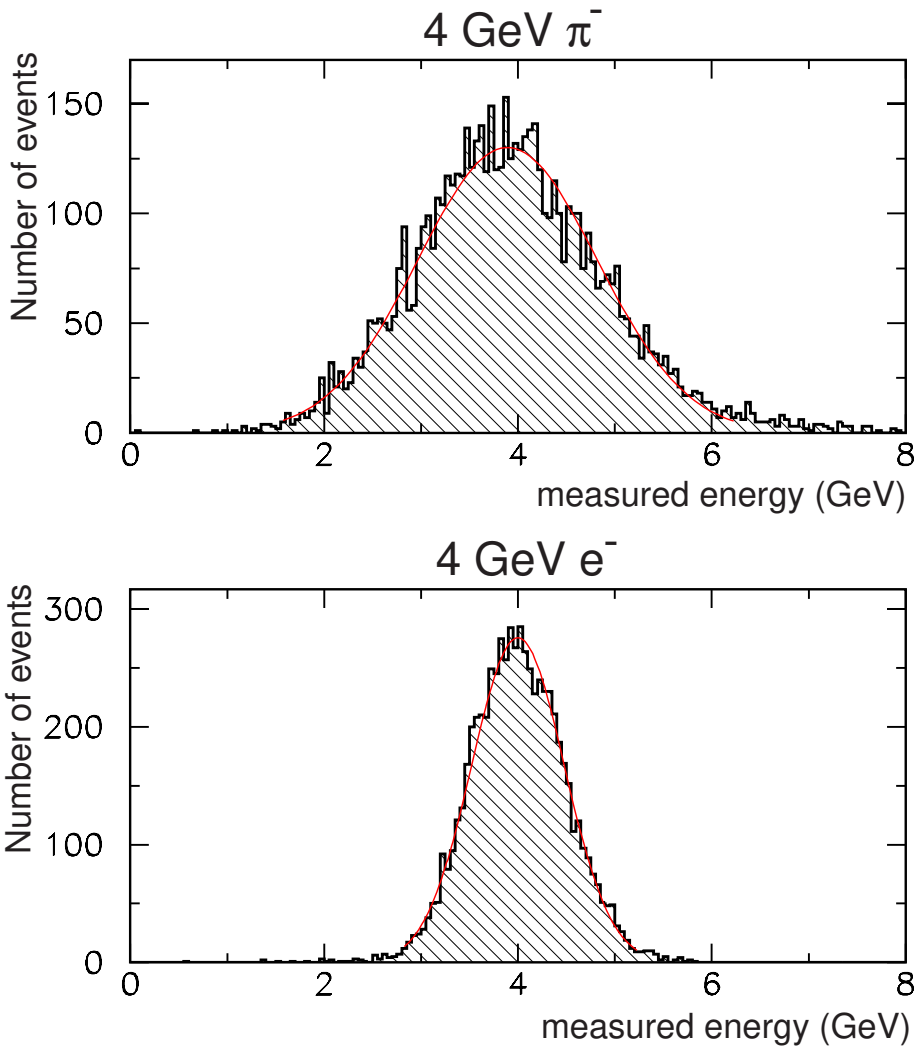

Figure 9: Measured energy spectrum for pions (upper) and for electrons (lower) in T411.

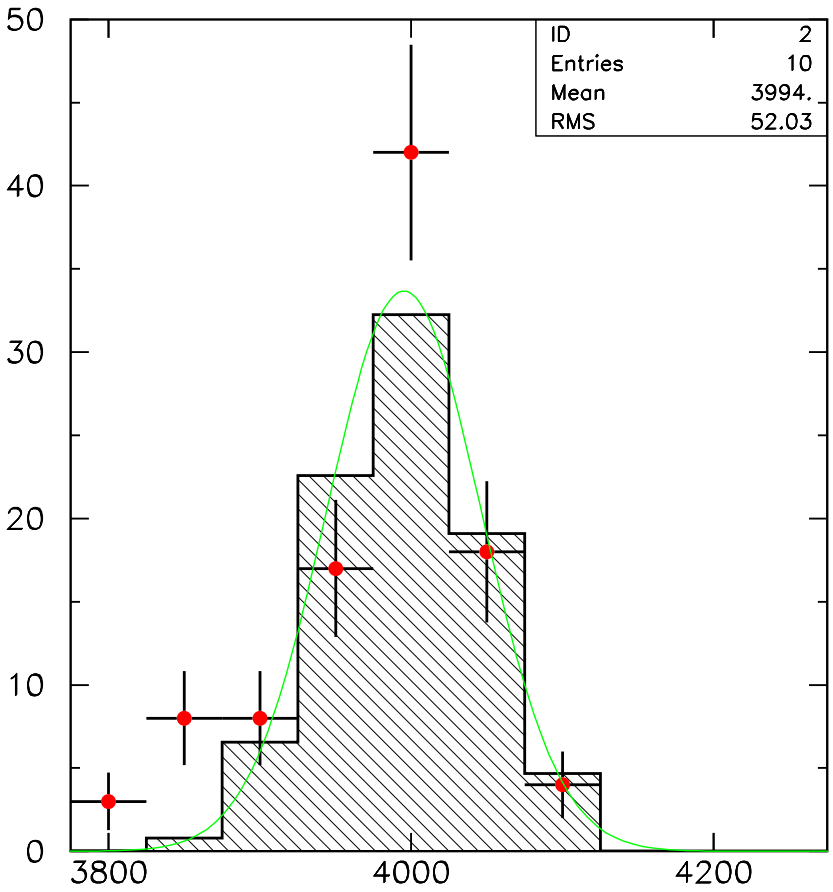

Figure 10: Distribution of lead plate thickness.

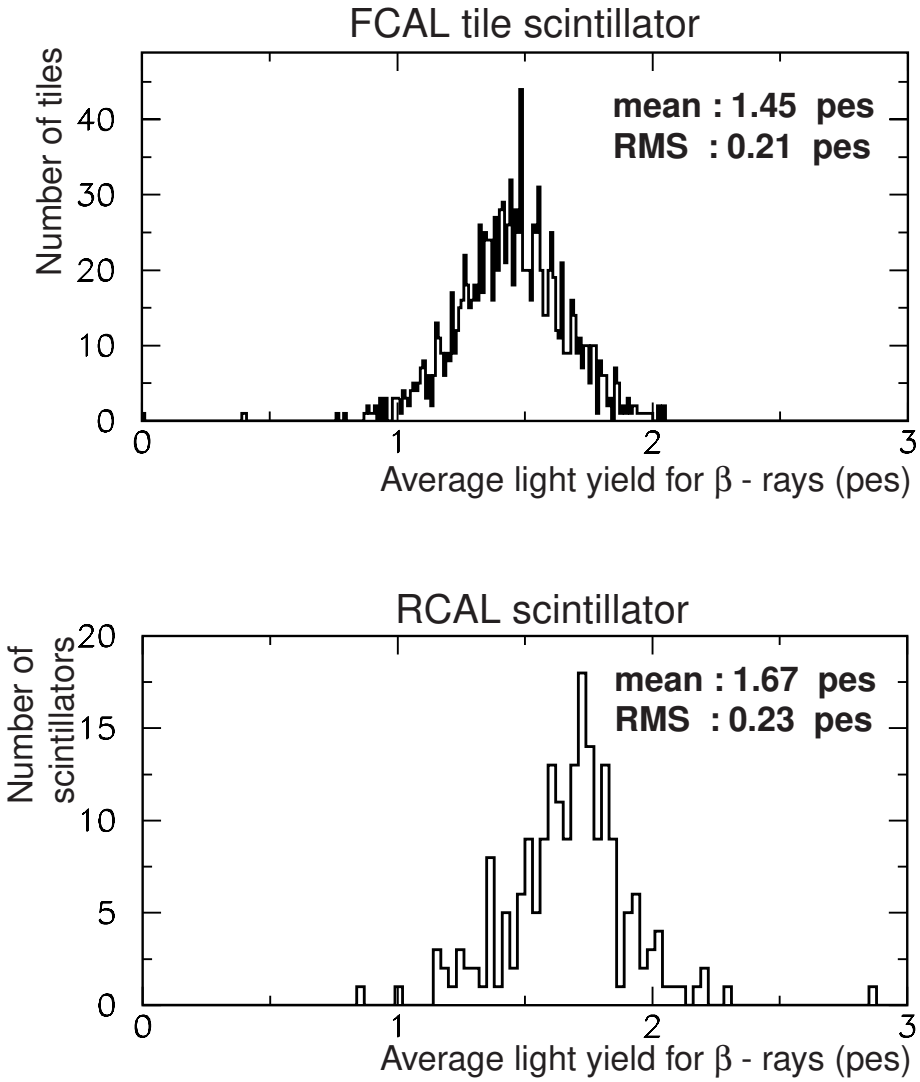

Figure 11: Photo-electron yield distribution of FCAL tiles (upper) and RCAL scintillator plates (lower) measured with β-rays. Unit of horizontal axis is photoelectrons.

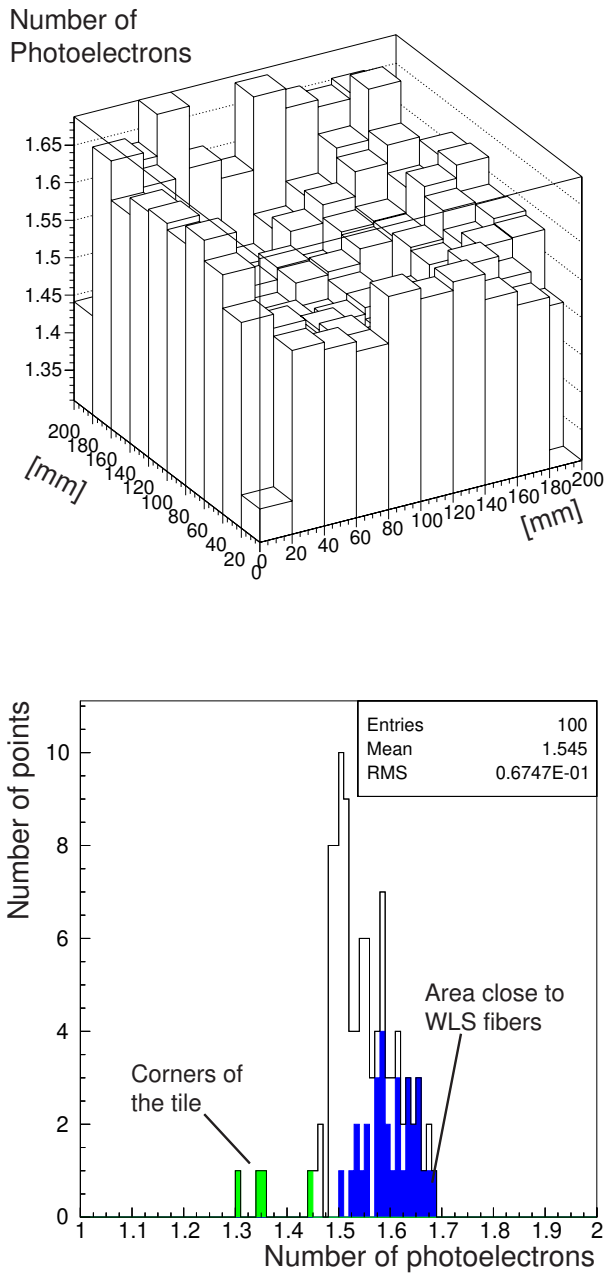

Figure 12: Uniformity of photo-electron yield over one scintillator tile. Upper is a map over a tile, and lower is its distribution.

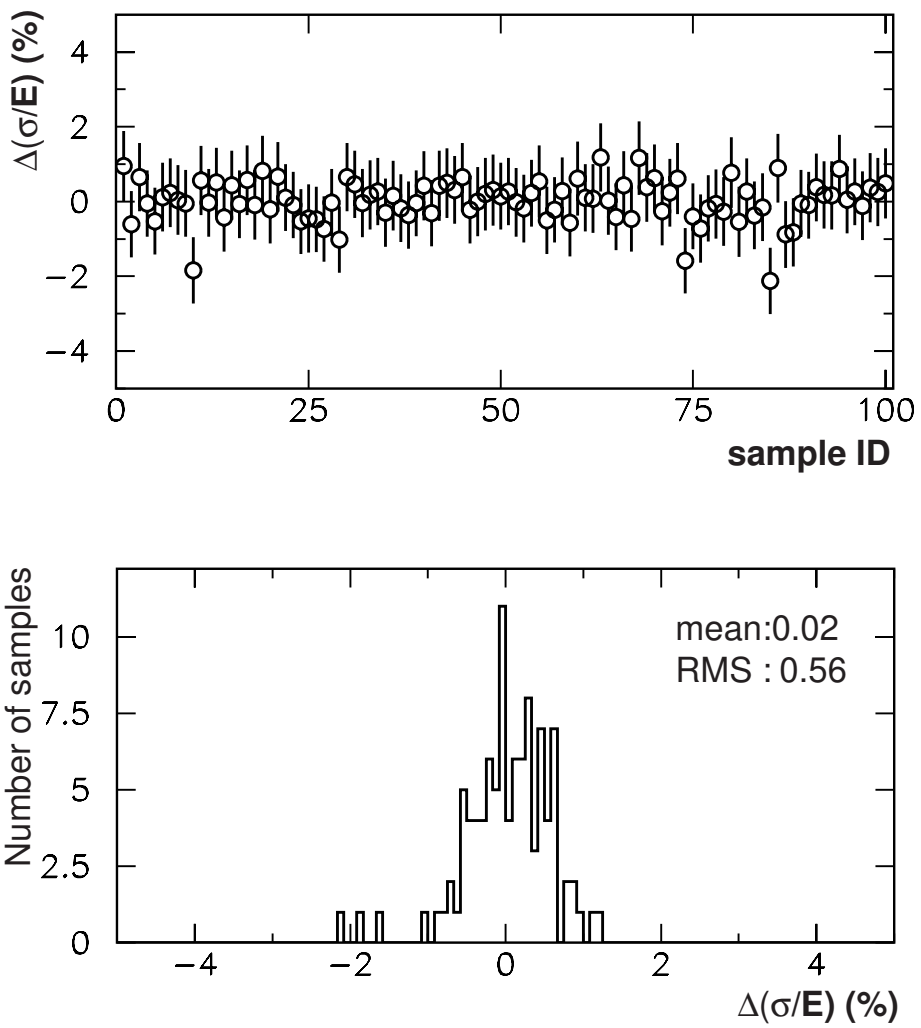

Figure 13: Effect of the variation of average photo-electron yield of scintillator tiles on the energy resolution. Upper is simulated energy resolution for 100 samples, and lower is its distribution.

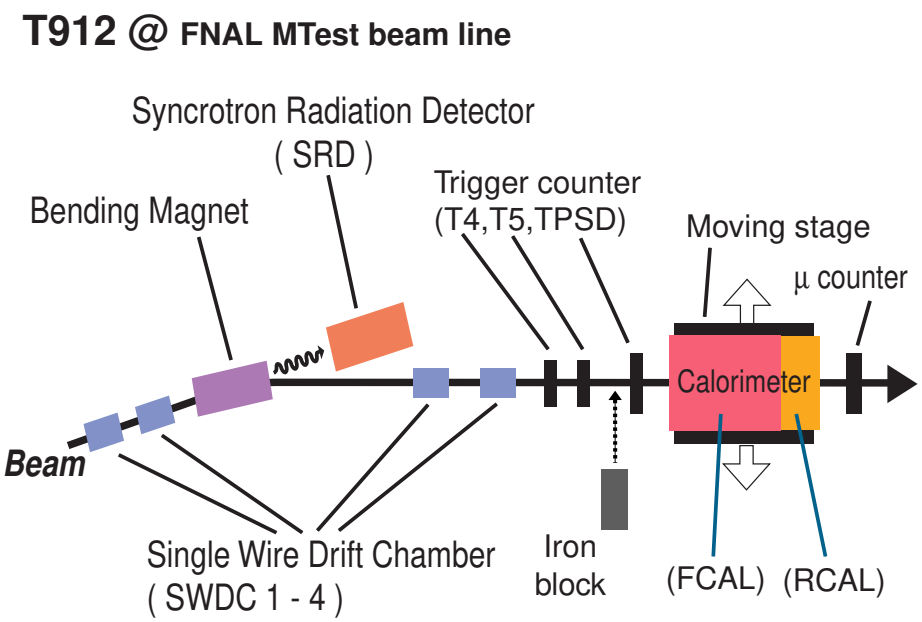

Figure 14: A schematic view of the T912 beam line setup.

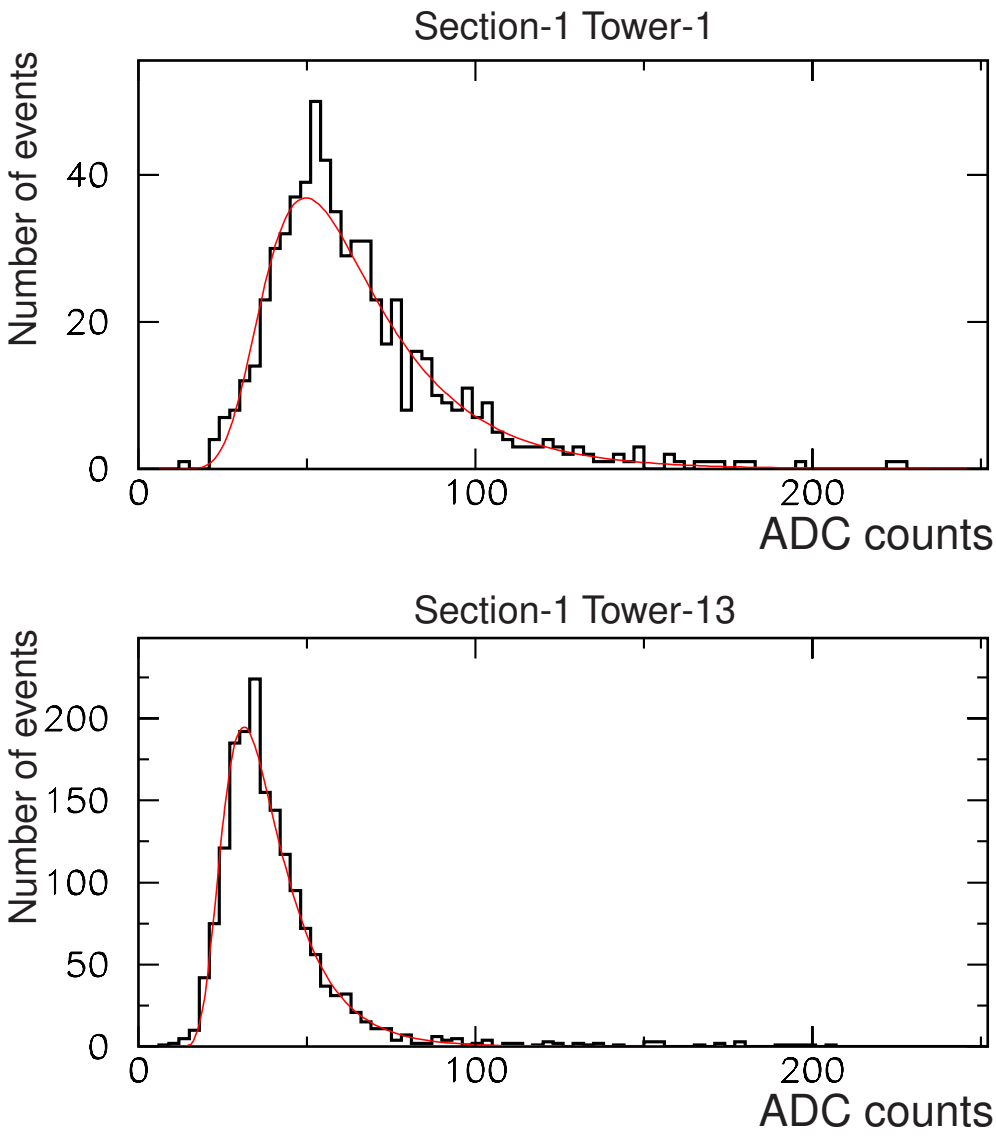

Figure 15: Typical spectrum of muons. Upper is for tower 1 at the corner, and lower is for tower 13 at the center.

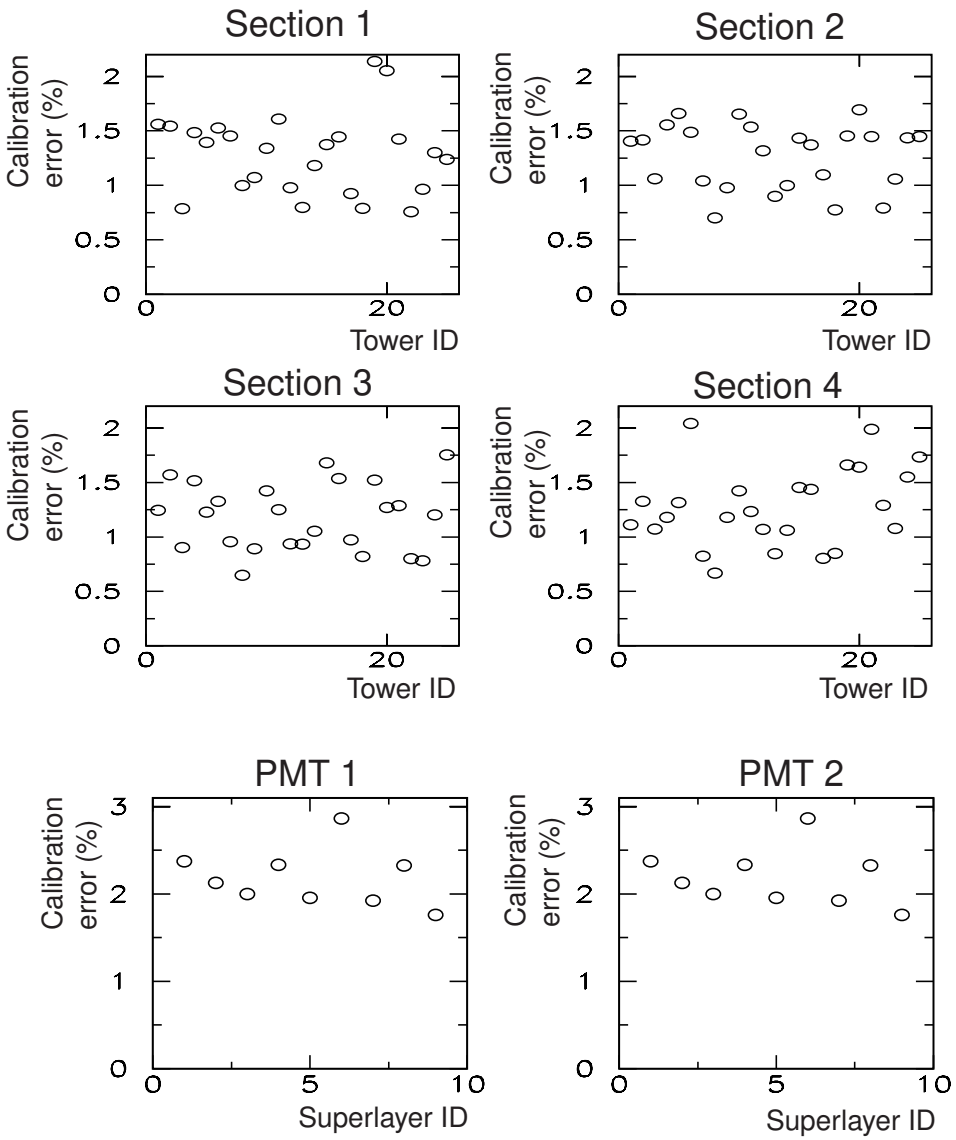

Figure 16: Stochastic error of calibration in T912.

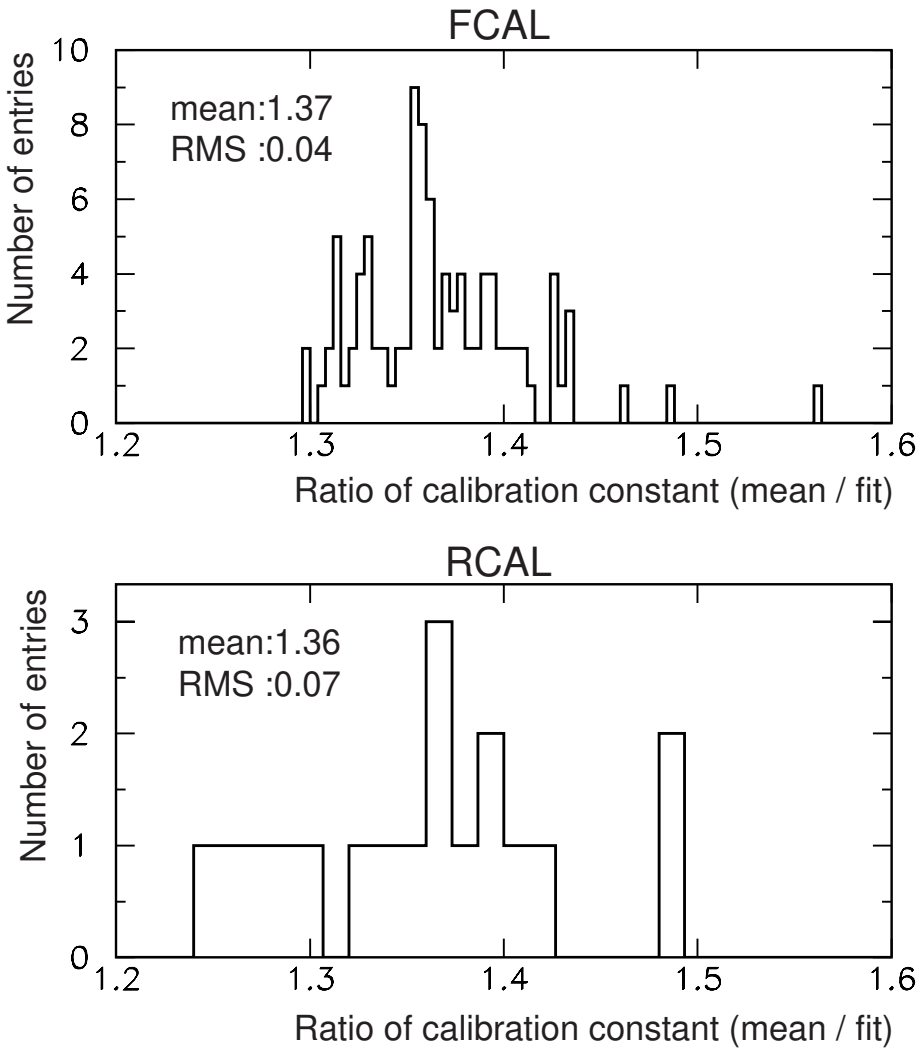

Figure 17: The distribution of ratio between calibration constant determined by numerical mean and determined by fit parameter.

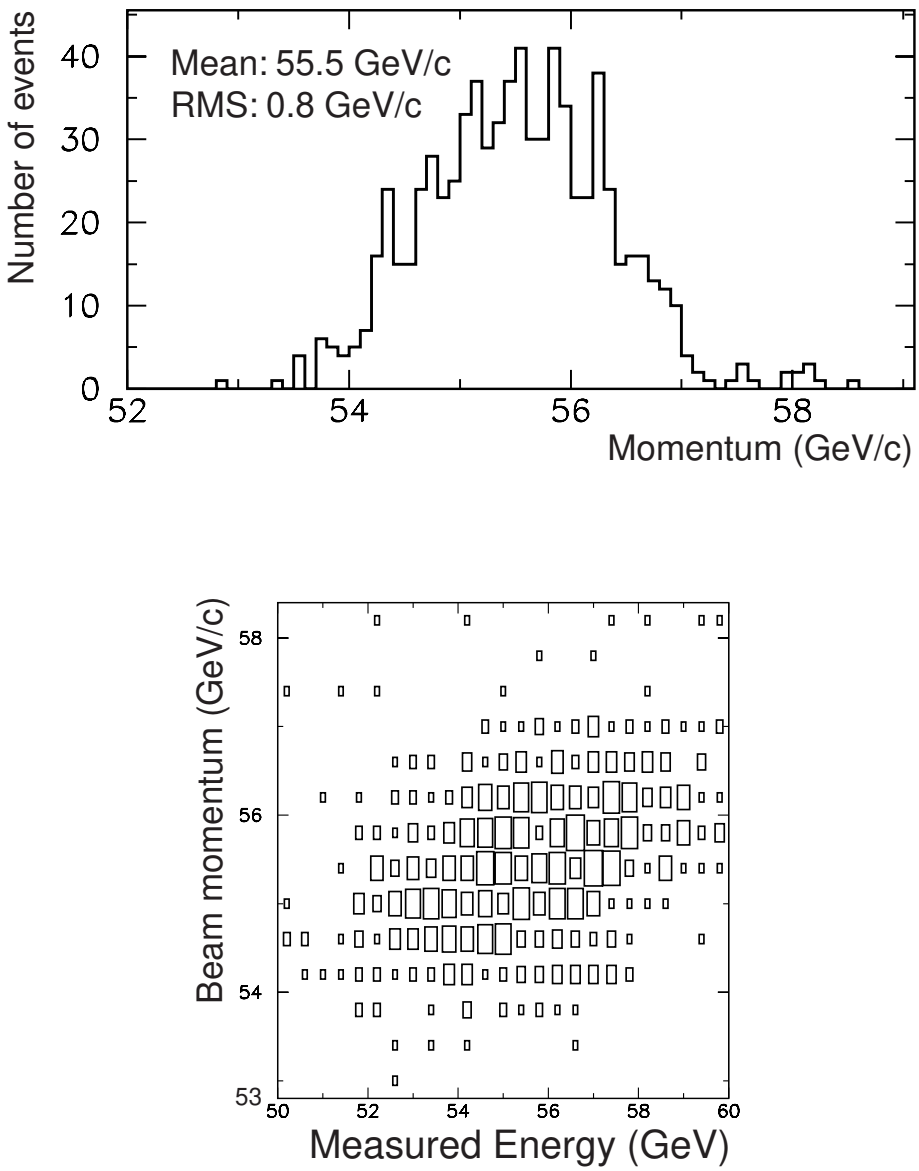

Figure 18: Reconstructed beam momentum distribution in T912 for electrons (upper), and correlation between particle momentum and energy measured by calorimeter.

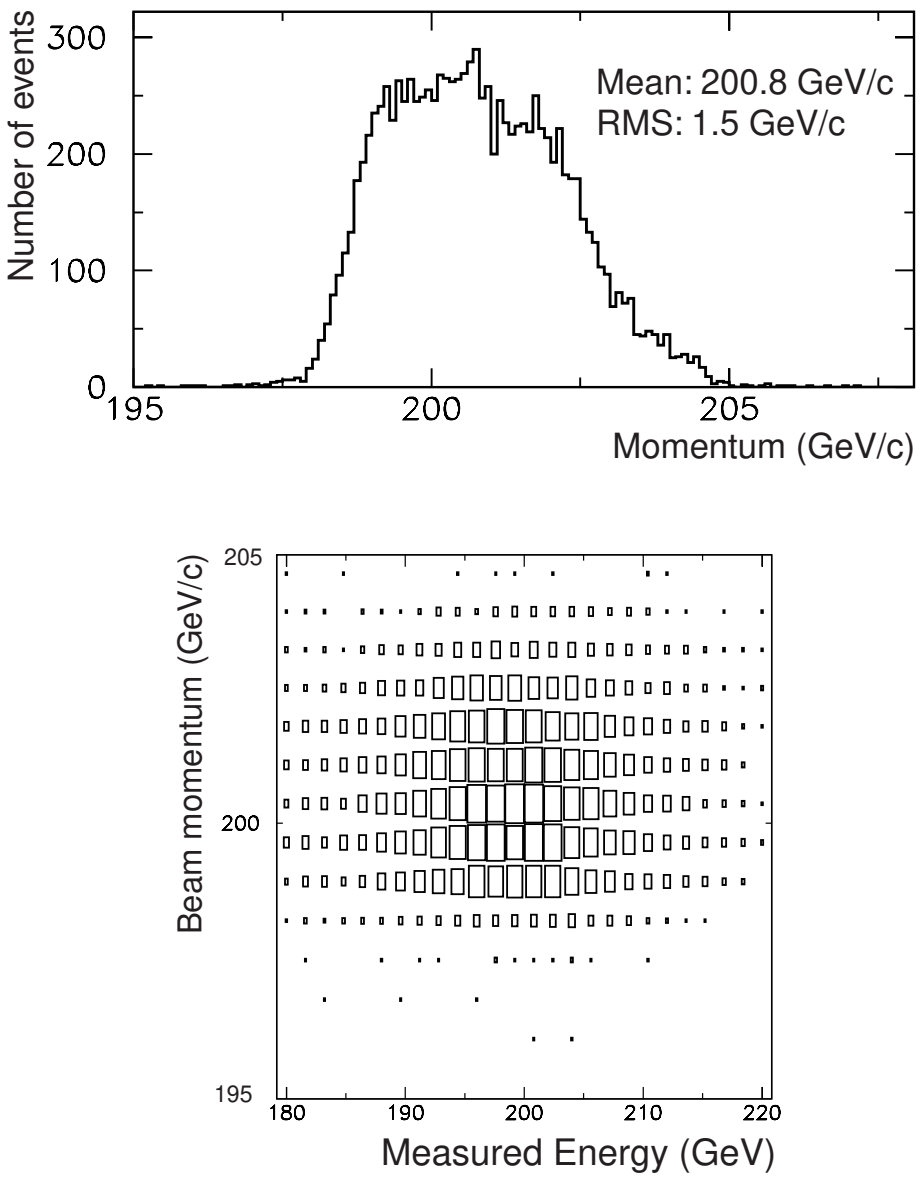

Figure 19: Reconstructed beam momentum distribution in T912 for pions (upper), and correlation between particle momentum and energy measured by calorimeter (lower).

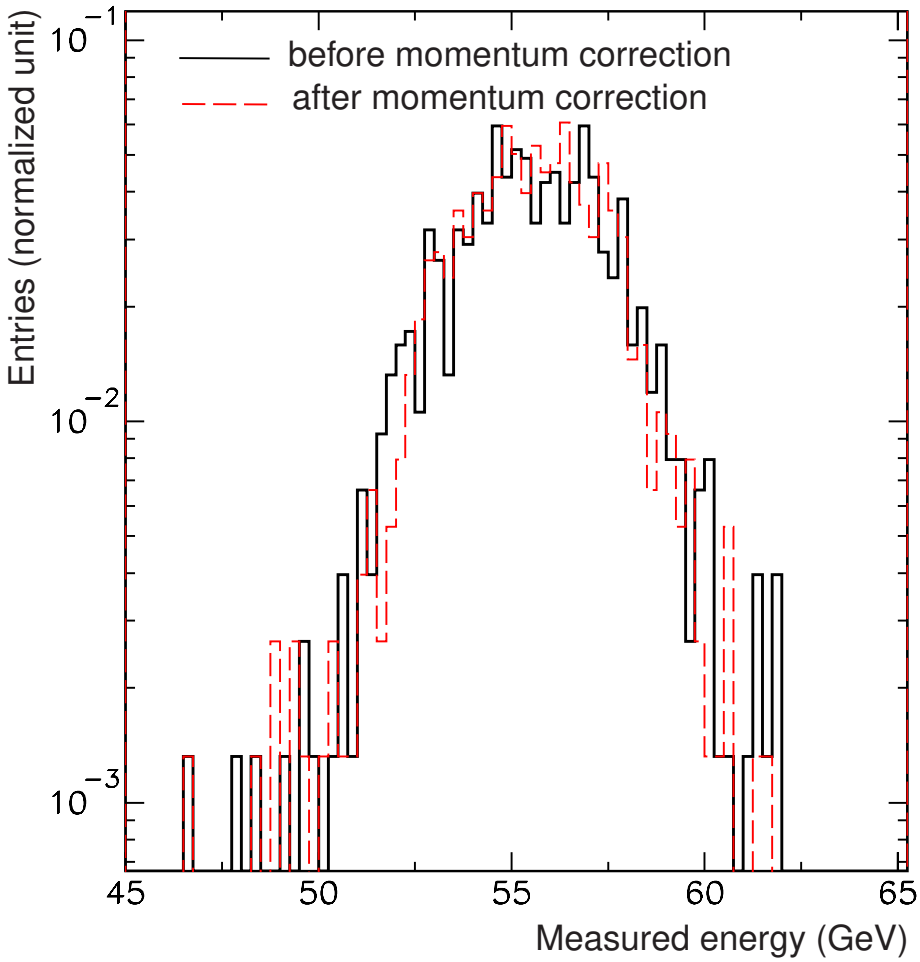

Figure 20: Calorimeter energy spectrum before and after event-by-event momentum correction for electrons.

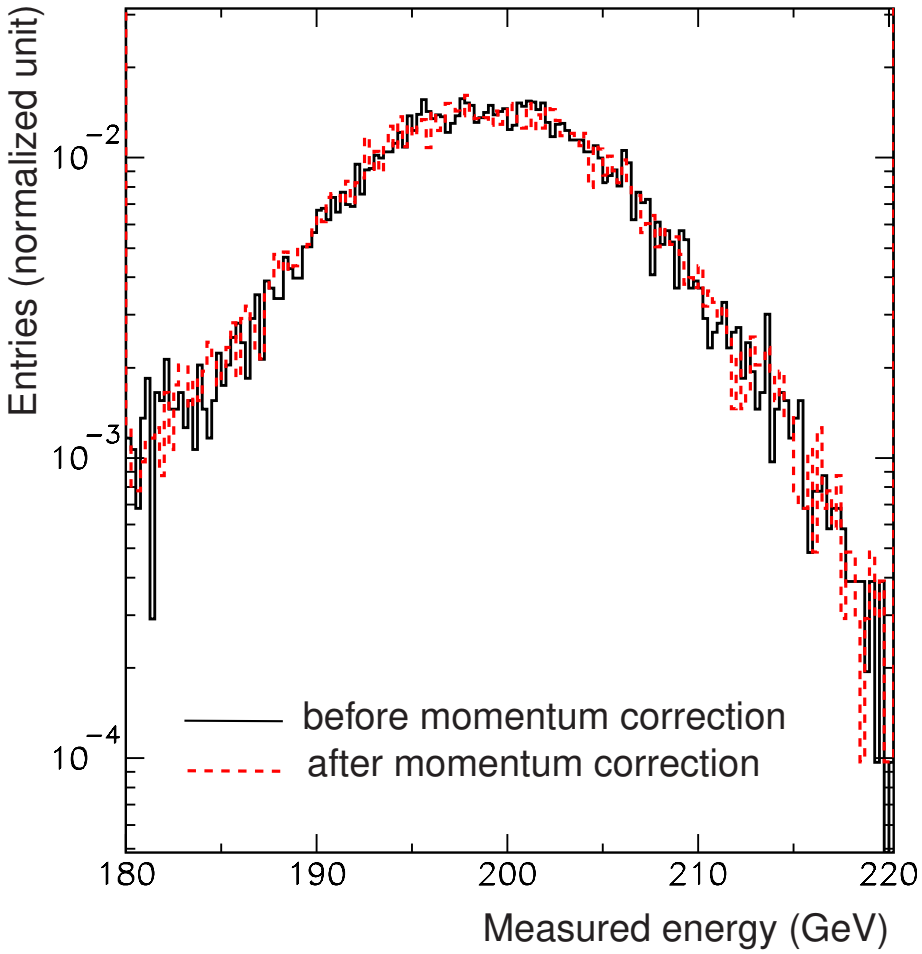

Figure 21: Calorimeter energy spectrum before and after event-by-event momentum correction for pions.

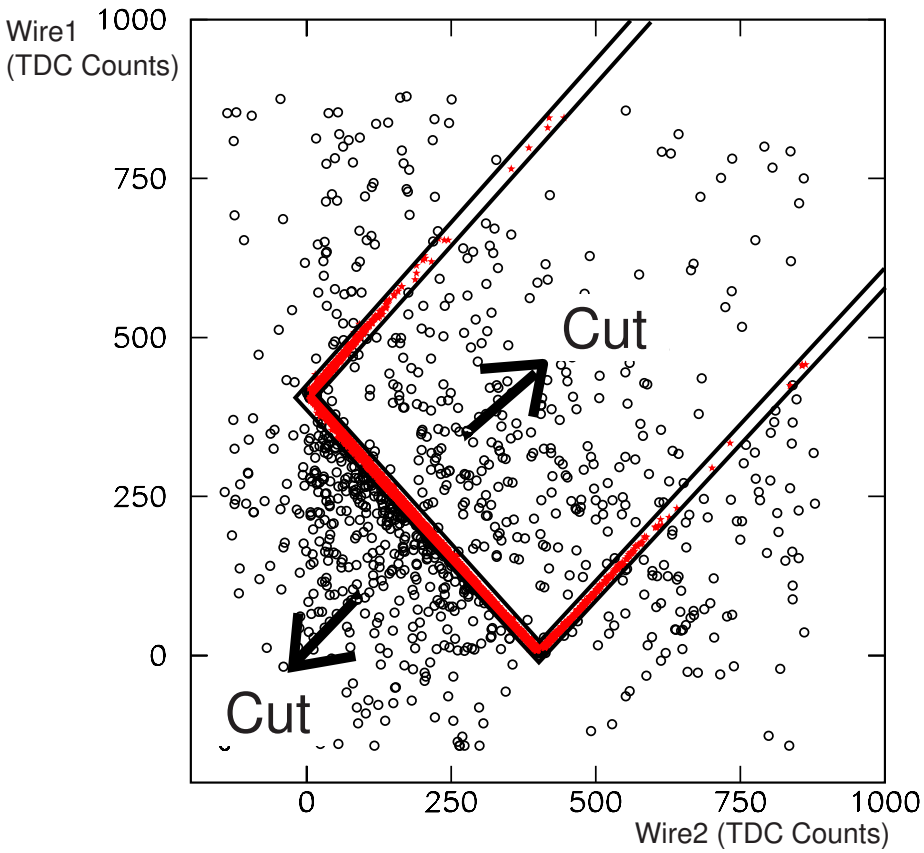

Figure 22: Scatter plot of TDC values for two successive SWDCs. Events between two lines are accepted.

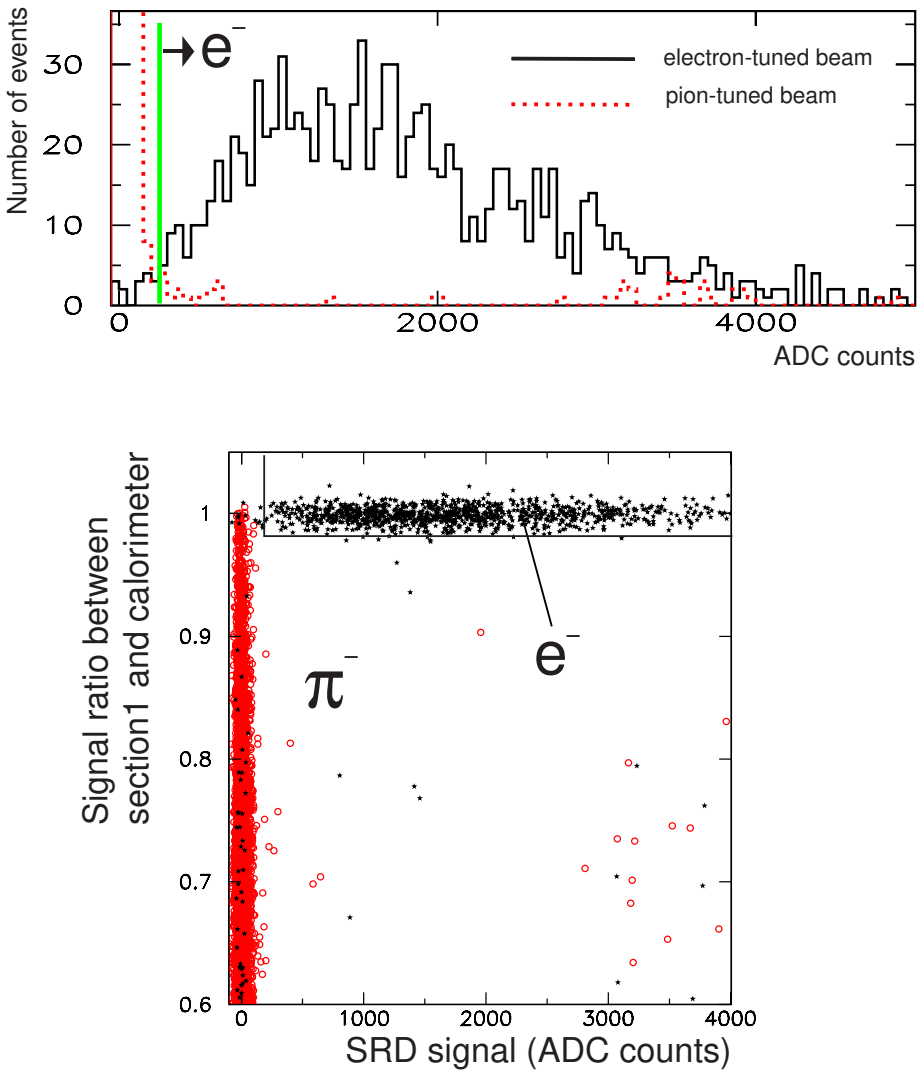

Figure 23: Pulse height spectrum of SRD for electron-tuned and pion-tuned beams (upper), and an example of electron selection using calorimeter and SRD signals.

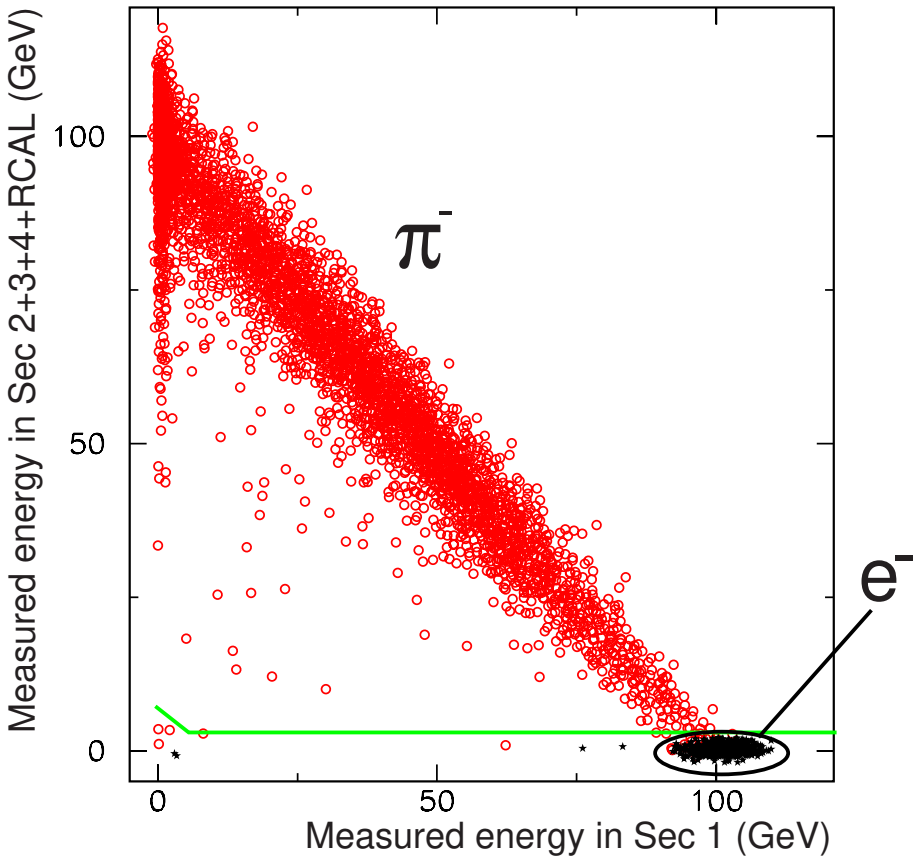

Figure 24: An example of electron and pion discrimination using calorimeter signals. Horizontal axis is energy deposit in section 1, and vertical axis is sum of energy deposit in other sections.

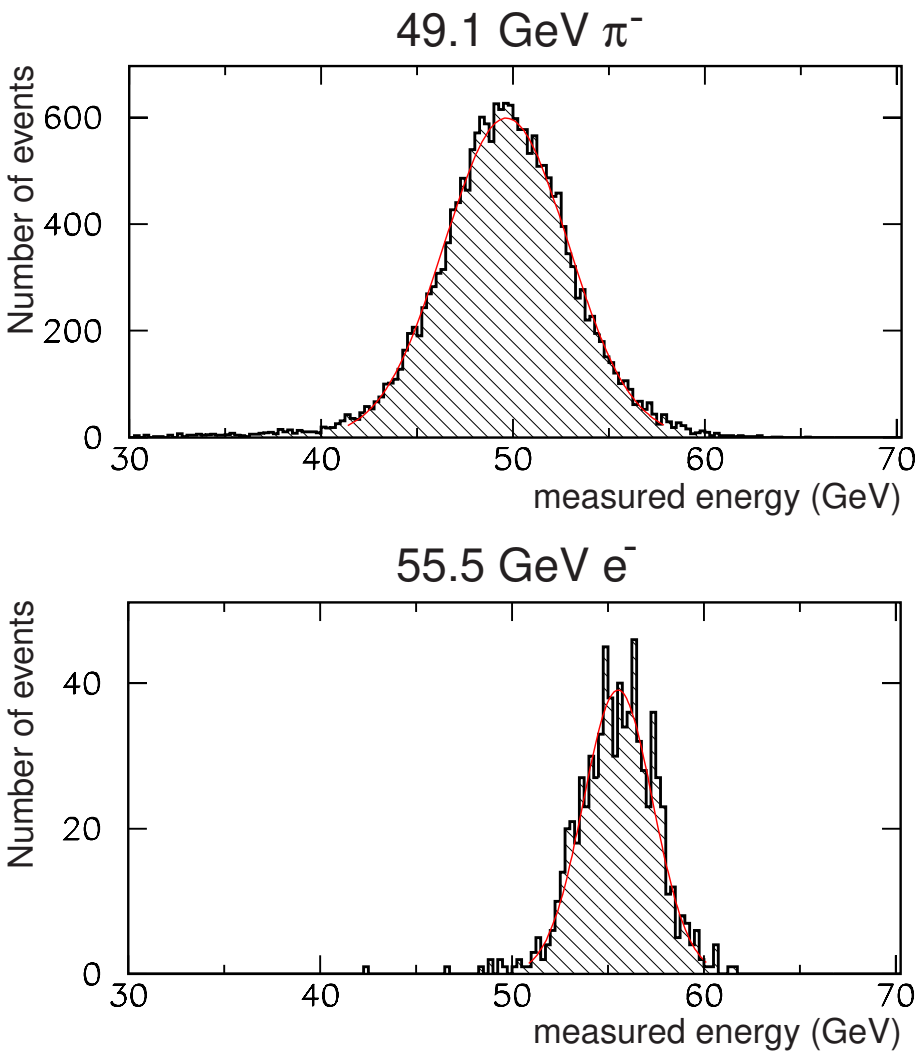

Figure 25: Typical energy spectrum in T912.

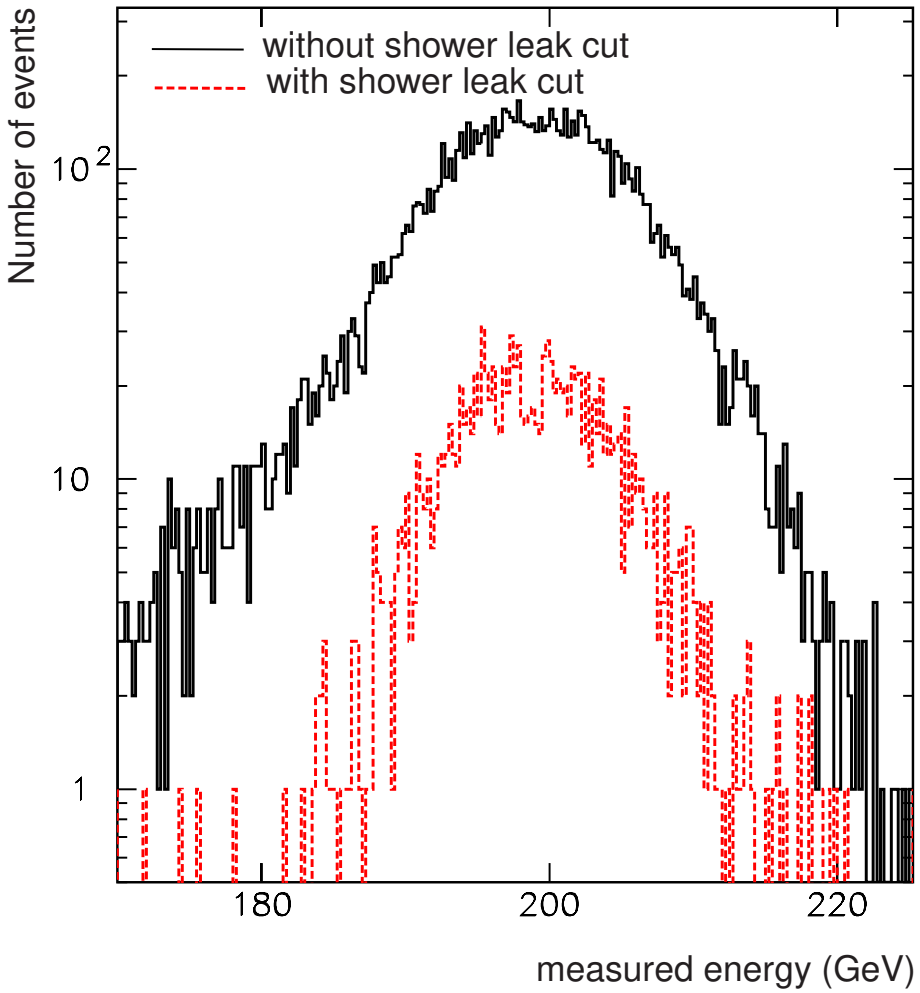

Figure 26: Comparison of pion energy spectra between with and without shower-leakage cut.

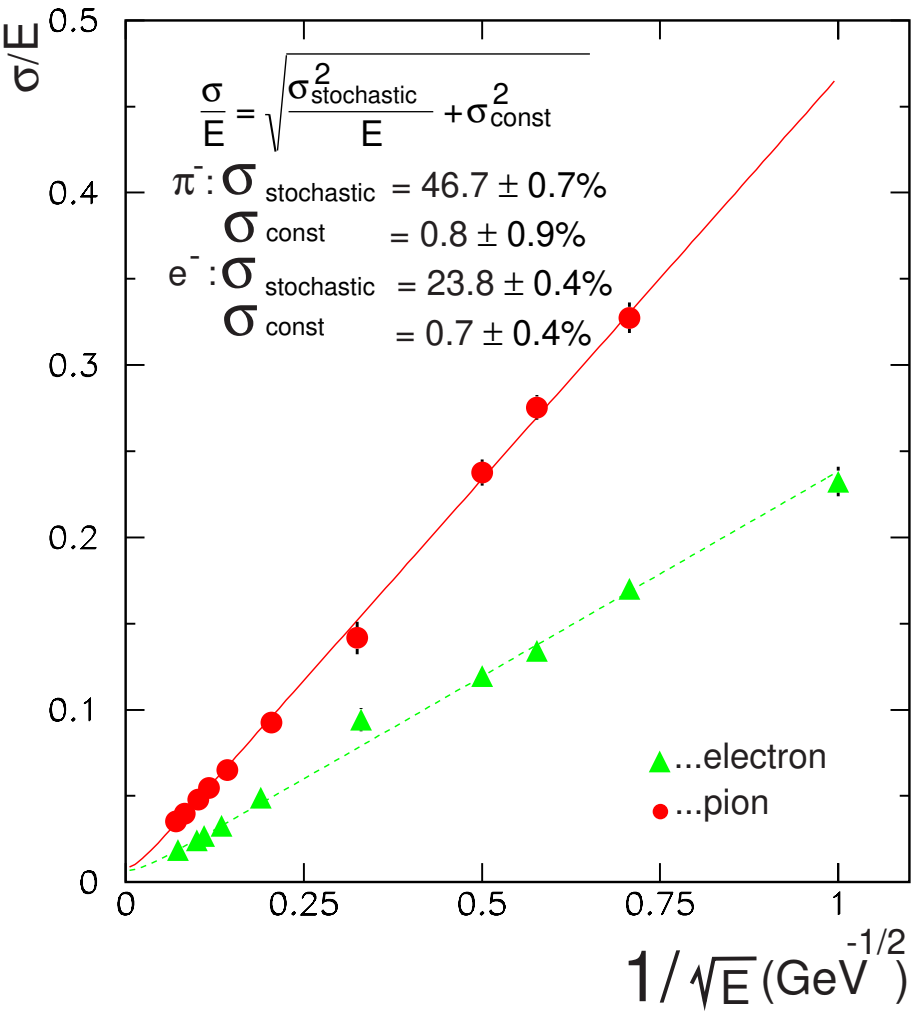

Figure 27: Energy resolution of calorimeter without shower-leakage cut.

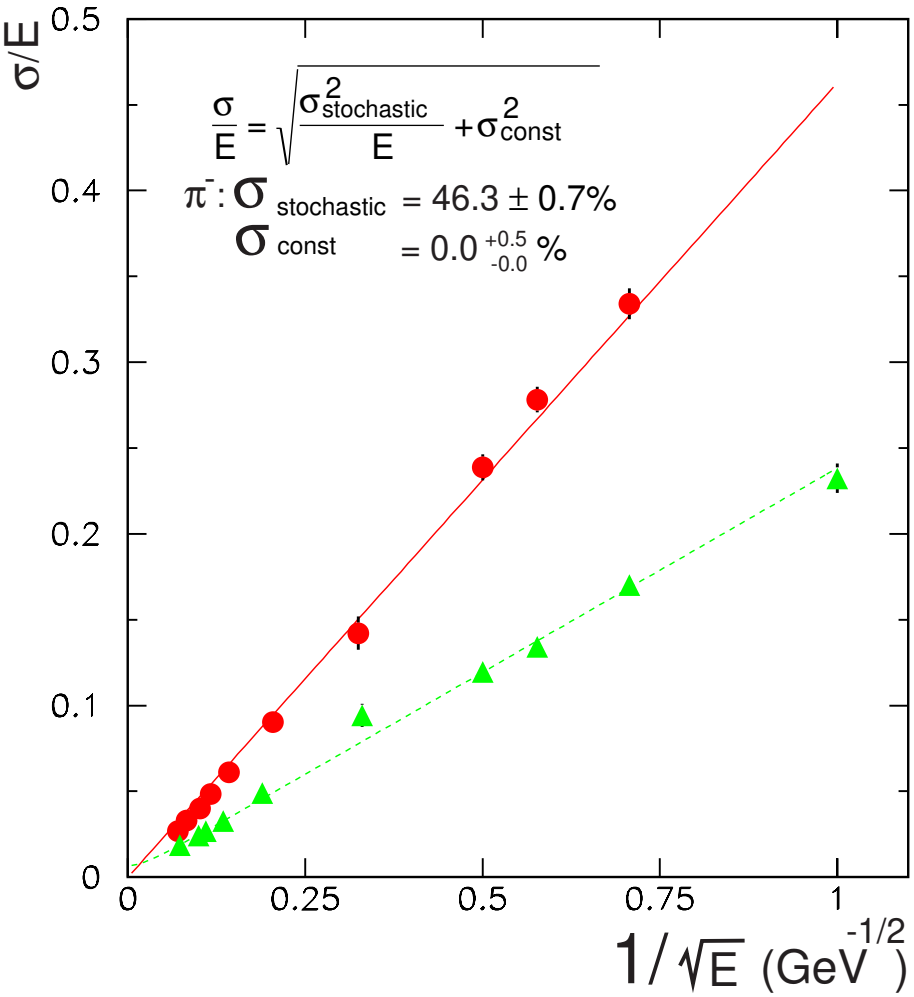

Figure 28: Energy resolution of calorimeter with shower-leakage cut.

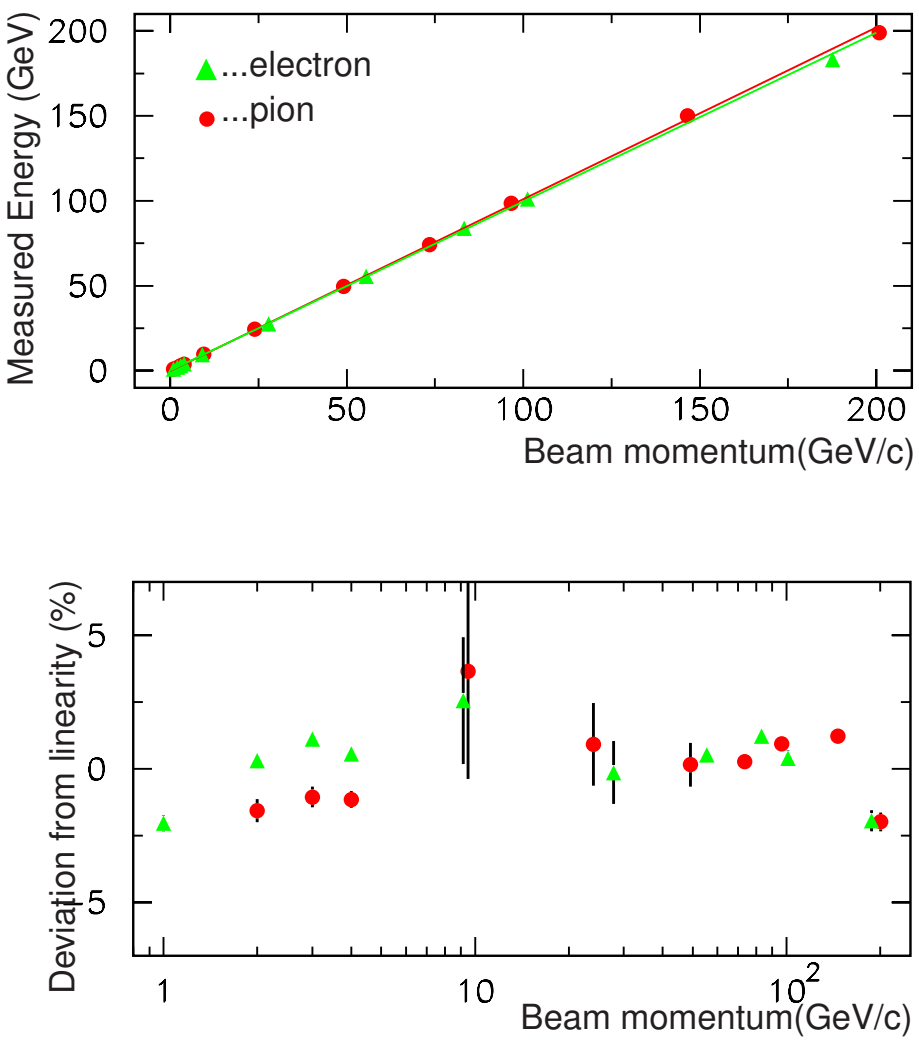

Figure 29: Linearity and deviation of calorimeter without shower-leakage cut.

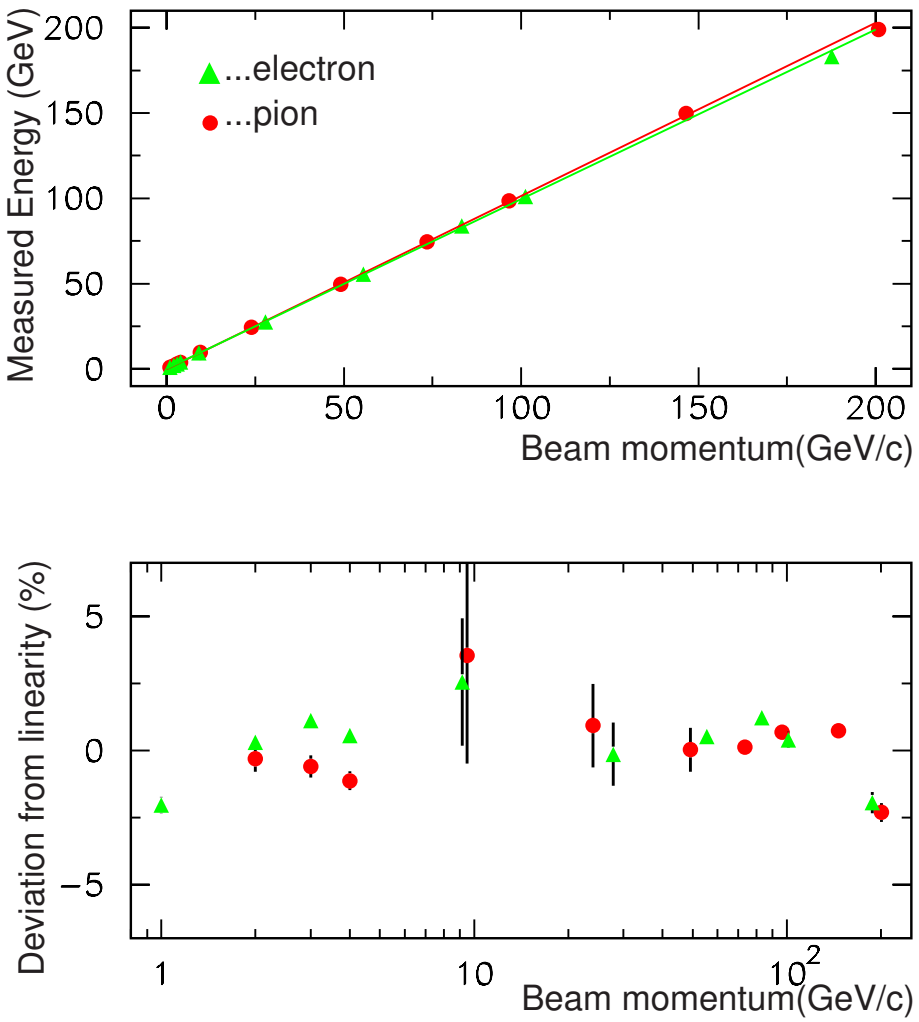

Figure 30: Linearity and deviation of calorimeter with shower-leakage cut.

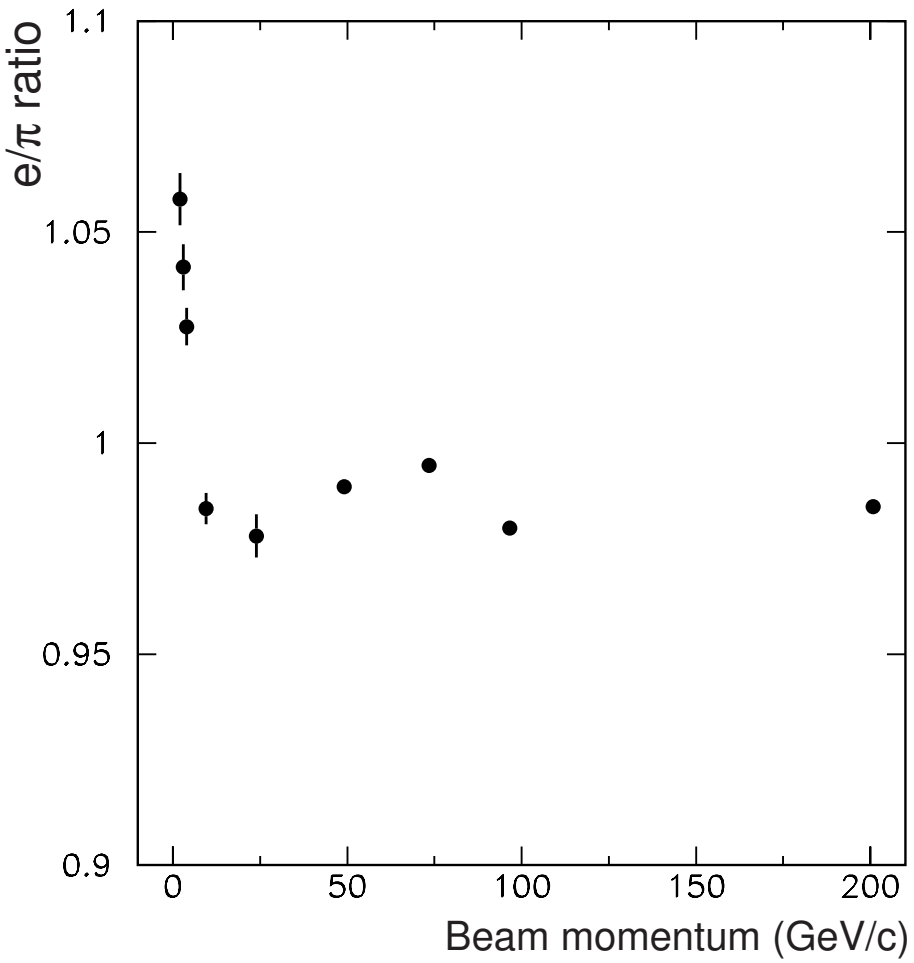

Figure 31: e/π ratio of calorimeter. (not a final plot)